Surface velocity fields of active rock glaciers and ice-debris complexes in the Central Andes of Argentina

Jan Henrik Blöthe,[1,2]* Christian Halla,[2] Ellen Schwalbe,[3] Estefania Bottegal,[4] Dario Trombotto Liaudat[4] and Lothar Schrott[2]
[1] Institute of Environmental Social Sciences and Geography, University of Freiburg, Freiburg, Germany
[2] Department of Geography, University of Bonn, Bonn, Germany
[3] Institute of Photogrammetry and Remote Sensing, Technische Universität Dresden, Dresden, Germany
[4] Geocryology, Instituto Argentino de Nivología, Glaciología y Ciencias Ambientales, CCT CONICET, Mendoza, Argentina

*Correspondence to: Jan H. Blöthe, Institute of Environmental Social Sciences and Geography, University of Freiburg, Schreiberstraße 20, 79085 Freiburg, Germany.
E-mail: jan.bloethe@geographie.uni-freiburg.de*

ESPL

Earth Surface Processes and Landforms

ABSTRACT: Rock glaciers and transitional ice-debris complexes predominate the Central Andean landform assemblage, yet regional studies on their state of activity and their kinematics remain sparse. Here we utilize the national glacier inventory of Argentina to quantify surface velocity fields of 244 rock glaciers and 51 ice-debris complexes, located in the Cordón del Plata range, Argentina. Applying a feature-tracking approach to repeated RapidEye satellite imagery acquired between 2010 and 2017/18, we find mean displacement rates between 0.37 and 2.61 m year^{-1} for 149 landforms, while for the remaining 146 features, surface movement remains below our level of detection. We compare our satellite-derived velocity fields with ground-truth data from two local field sites and find closely matching results in magnitude and spatial distribution. With average displacement of one-third of the active rock glaciers and ice-debris complexes exceeding 1 m year^{-1}, the region hosts an exceptional number of fast-flowing periglacial landforms, compared to other mountain belts. Using a random forest model, we test the predictive power of 25 morphometric and topoclimatic candidate predictors for modelling the state of activity of rock glaciers and ice-debris complexes on two different scales. For entire landforms and individual landform segments, constructed along displacement centrelines, we can predict the state of activity with overall accuracies of 70.08% (mean AUROC = 0.785) and 74.86% (mean AUROC = 0.753), respectively. While topoclimatic parameters such as solar radiation and elevation are most important for entire landforms, geometric parameters become more important at the scale of landform segments. Despite tentative correlations between local slope and surface kinematics, our results point to factors integrating slope and distance to the source to govern local deformation. We conclude that feature tracking in optical imagery is feasible for regional studies in remote regions and provides valuable insight into the current state of the Andean cryosphere. © 2020 The Authors. Earth Surface Processes and Landforms published by John Wiley & Sons Ltd

KEYWORDS: rock glaciers; ice-debris complexes; permafrost; feature tracking; centreline modelling; random forests; Central Andes; RapidEye

Introduction

High mountain environments often serve as water towers for their adjacent lowlands (Viviroli and Weingartner, 2004). This is especially true for arid to semi-arid mountain ranges, such as the Central Andes (30–33°S), where human livelihoods critically depend on meltwaters from snow and ice (Kaser *et al.*, 2010; Falaschi *et al.*, 2014). In the light of recent global warming, a thorough database on high mountain water resources is a prerequisite for the development of suitable adaptation strategies (Viviroli *et al.*, 2011). Apart from glaciers, whose role in storing water and contributing to mountain river discharge has long been studied (Kaser *et al.*, 2010), there is growing evidence that the assemblage of periglacial landforms with its invisible underground ice resources also plays an important role in mountain hydrology (Rangecroft *et al.*, 2013; Pourrier *et al.*, 2014; Haeberli *et al.*, 2017).

Earlier studies reported an exceptional density of periglacial landforms in the Central Andes of Argentina and Chile (Paskoff, 1970; Corte, 1976; Brenning, 2005), coinciding with the most extensive periglacial belt modelled for the Southern Hemisphere outside Antarctica (Gruber, 2012). In contrast to the European Alps, rock glaciers predominate in the landscape and often outnumber glaciers in the Central Andes, with individual forms frequently exceeding 10^6 m^2 (IANIGLA, 2018d). This observation spurred an ongoing debate regarding the hydrological significance of rock glaciers in the region (Corte, 1976; Arenson and Jakob, 2010; Azócar and Brenning, 2010; Jones *et al.*, 2018; Schaffer *et al.*, 2019) that calls for further studies of the hydrological resources of the Andes.

Acknowledging this, the Argentinian government issued a law in 2010 that called for the conservation of the glacial and periglacial environment alike, both constituting important hydrological resources in the Andes. Recently, Argentina published its national glacier inventory (Inventario Nacional de Glaciares, ING) that is subdivided into 69 subregions and comprises more than 16 000 ice-containing landforms with a minimum surface area of 0.01 km^2 (IANIGLA, 2018d). Based on supervised classification (clear ice landforms) and visual interpretation (debris-covered landforms) of optical remote-sensing imagery and digital elevation models (IANIGLA, 2018d), the ING discriminates five different classes of cryogenic landforms: glaciers, permanent snow patches, debris-covered glaciers, rock glaciers, and ice-debris complexes (Table 1). The terminology of the ING is largely based on the guidelines from the Global Land Ice Measurements from Space (GLIMS) programme (Rau et al., 2005), with some adaptations made to reflect the variety of periglacial landforms within the Andes.

Commonly, rock glaciers are classified into three groups (Barsch, 1996). Landforms with ongoing movement due to the plastic deformation of internal ice, often expressed in a pronounced ridge and furrow topography, are classified as active. Rock glaciers that still contain ice in their interior, but with no indication of active movement, are classified as inactive. While active and inactive landforms, collectively referred to as intact, belong to the phenomenon of alpine permafrost, relict (or fossil) rock glaciers do not have a frozen core and can be seen as indicators of past climatic conditions. Inventories of intact rock glaciers are therefore valued as indicators of the current permafrost distribution in alpine settings (Boeckli et al., 2012; Schrott et al., 2012; Scotti et al., 2013; Saito et al., 2016).

Even though rock glaciers are not usually considered to be part of the assemblage of glacial landforms (Haeberli, 1985; Barsch, 1996), some national and international inventories include them in their classification (Rau et al., 2005; Barcaza et al., 2017; IANIGLA, 2018d), recognizing their hydrological importance. There is an ongoing debate on where to draw the terminological line between rock glaciers from a purely periglacial origin and rock glaciers involving a glacigenic ice contribution, culminating in what has been referred to as the 'rock glacier controversy' (Berthling, 2011). While both positions acknowledge the presence of a continuum between the glacial and periglacial landforms (Potter, 1972; Barsch, 1996; Humlum, 2000; Haeberli et al., 2006), the discussion centres around the question of whether (debris-covered) glaciers that grade into landforms with similar surface morphology and kinematics as rock glaciers should be classified as such. As a step

forward, Berthling (2011, p. 103) proposes a more universal definition of active rock glaciers as 'the visible expression of cumulative deformation by long-term creep of ice/debris mixtures under permafrost conditions', including the processes responsible for movement, but avoiding any statement on the origin of the material involved. Though not explicitly citing Berthling (2011), but largely following the proposed definition, the ING allows for glacial and non-glacial ice origin in rock glaciers, as well as a combination of both sources in single landforms, and assigns all of these landforms to the same class. In arid to semi-arid mountain ranges, however, a clear distinction is often complicated by the juxtaposition of debris-covered glaciers, moraine complexes and rock glaciers (Janke et al., 2015; Monnier and Kinnard, 2015; Bolch et al., 2019). Here we adopt the term 'ice-debris complex' as an umbrella for such landforms that contain elements of debris-covered glaciers that grade into rock glaciers in their lower parts (IANIGLA, 2018d; Bolch et al., 2019), a form frequently found in the Central Andes (Bodin et al., 2010; Monnier and Kinnard, 2015).

Active movement of rock glaciers and ice-debris complexes is primarily associated with the plastic deformation of interstitial and excess ice under the force of gravity (i.e. permafrost creep) (Kääb et al., 2003; Haeberli et al., 2006) and the movement along a basal shear horizon (Arenson et al., 2002; Kenner et al., 2017). While permafrost creep has been modelled successfully by adapting Glen's flow law (Konrad et al., 1999), differences in local slope, permafrost thickness and material density are not able to fully explain the spatial pattern of rock glacier movement (Haeberli, 1985; Haeberli et al., 2006). Observations of a seasonal cyclicity of permafrost creep identified the importance of liquid water availability and air temperature (as a proxy for internal temperature) on rock glacier kinematics (Kääb et al., 2007; Kenner et al., 2017); other studies find a series of topographic and geometric parameters that correlate with surface velocities (Frauenfelder et al., 2003; Janke and Frauenfelder, 2008).

Despite the growing availability of rock glacier inventories and remote-sensing data with high spatio-temporal resolution, only a few studies are available that thoroughly investigate rock glacier kinematics and their controlling factors in a regional context (Liu et al., 2013; Wang et al., 2017; Groh and Blöthe, 2019), let alone exploring the within-landform variability of surface deformation.

We take the opportunity of the recently published ING (IANIGLA, 2018d) and aim to objectively quantify the surface displacement of rock glaciers and ice-debris complexes in a regional remote-sensing-based analysis. Further exploring this

Table 1. Terminology and explanations from the national glacier inventory of Argentina (Castro et al., 2014; IANIGLA, 2018d)

Translated terminology (this study)	Spanish terminology (IANIGLA inventory)	Description (IANIGLA inventory)
Glacier	Glaciar descubierto	Body of permanent ice that shows signs of active movement under the force of gravity. Glacier ice generated from recrystallization and compaction of snow and/or ice, the surface shows no significant debris coverage.
Permanent snow patch	Manchón de nieve	Permanent ice bodies generated from recrystallization and compaction of snow and/or ice with no signs of active movement or significant debris coverage at the surface.
Debris-covered glacier	Glaciar cubierto	Like glaciers, but with significant debris coverage at the surface.
Rock glacier	Glaciar de escombros	Body of frozen debris and ice that show signs of active movement under the force of gravity. The ice contained can be of glacial and non-glacial origin; active and inactive forms are classified, fossil forms are not contained in the inventory.
Ice-debris complex	Glaciar cubierto con glaciar de escombros	Debris-covered glaciers that gradually transition into rock glaciers. These forms are very common in the Andes and the exact limit between the glacial and periglacial domain is difficult to determine.

data set, we qualitatively analyse the spatial variability of surface deformation within individual landforms and try to identify key factors controlling the landforms' state of activity at different scales. Using a random forest classification approach, we test the predictive power of a set of morphometric and topoclimatic metrics to separate actively moving landforms and landform segments from their inactive counterparts.

Study Area

Our study area lies in the semi-arid Central Andes that are characterized by an extensive periglacial belt, in parts exceeding 2000 m vertical extent. Here, Andean meltwaters fuel the irrigation farming of the arid lowland regions around the population centres of Santiago de Chile and Mendoza (Falaschi et al., 2014). Within this region, the prevalence of periglacial landforms led to early investigations on the hydrological significance of rock glaciers in semi-arid mountain regions (Corte, 1976). Corte and Espizua (1981) created a first inventory of glacial and periglacial landforms in the region, finding one of the highest densities of cryo-conditioned landforms

worldwide (see Blöthe et al., 2019 for a global compilation of rock glacier densities).

On the eastern side of the Central Andes, the frontal cordillera rises sharply to almost 6 km in elevation in the Cordón del Plata range between 32.3 and 33.2°S, only ~65 km southwest of the city of Mendoza, Argentina (Figure 1). The Cordón del Plata range that covers ~2500 km^2 forms part of the Frontal Cordillera that is sandwiched between the Principal Cordillera in the West and the Precordillera in the East. Predominant fault orientation follows the general N–S alignment of the Andes, perpendicular to the predominant direction of the collision of the Nazca and South America plates (Montgomery et al., 2001). The basement of the Frontal Cordillera consists of Proterozoic to Palaeozoic metamorphic rocks, overlain by Permian to Triassic volcanic and plutonic rocks that are exposed in the northern and eastern part of the Cordón del Plata and Carboniferous sedimentary rocks predominating in the southern and southwestern part (Heredia et al., 2012; https://sigam.segemar.gov.ar). Though data coverage is sparse and records are often incomplete, mean annual precipitation was ~400 mm year^{-1} between 1979 and 2015, mean annual air temperature at 2550 m a.s.l. was 6.1 °C between 1979 and
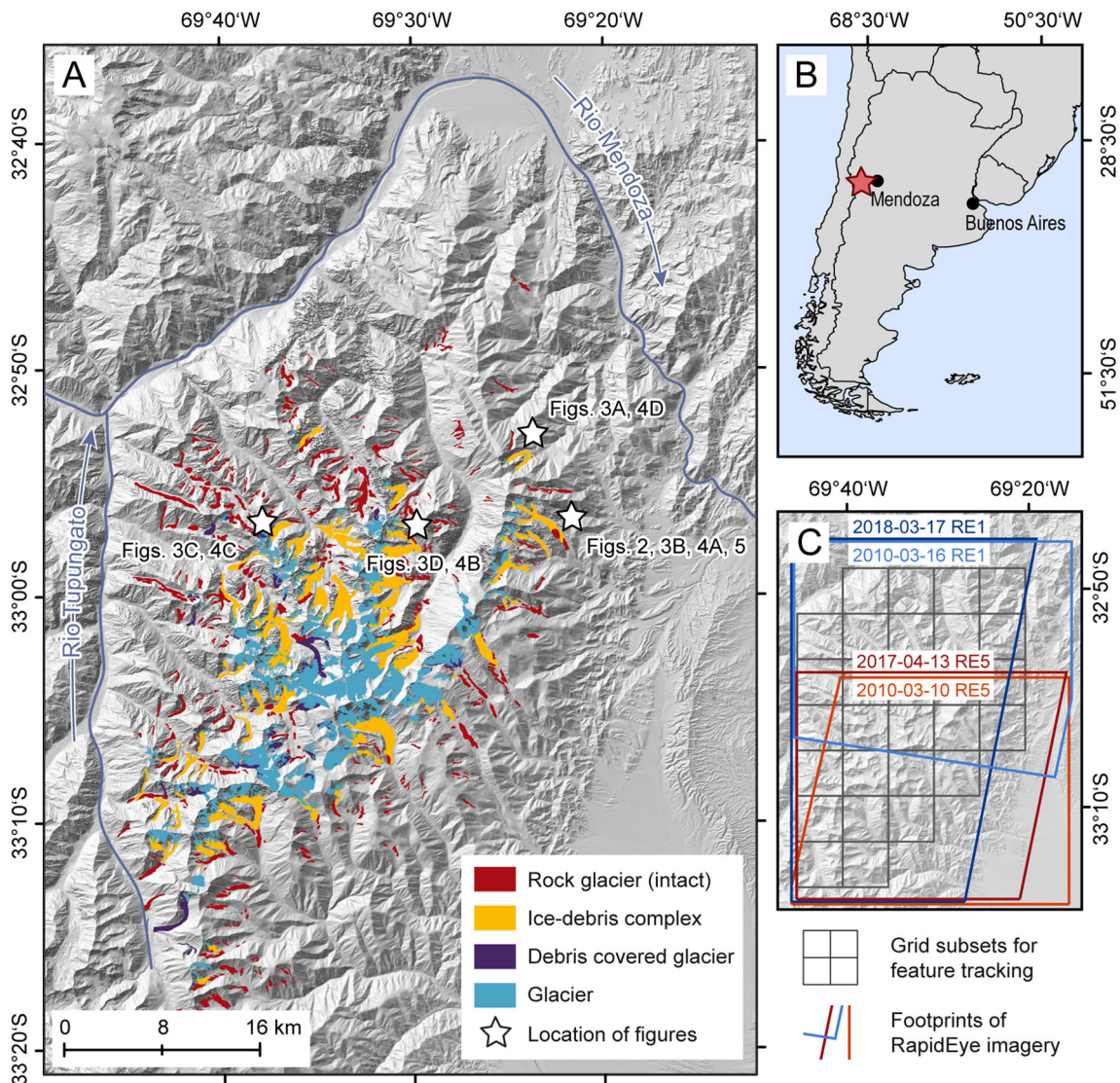

Figure 1. (A) Cordón del Plata range with 900 cryo-conditioned landforms [glaciers (287), debris-covered glaciers (57), ice-debris complexes (81) and intact (475) rock glaciers] contained in the national glacier inventory of Argentina (www.glaciaresargentinos.gob.ar). White stars indicate location of figures. (B) Location map of southern South America with the study area indicated by the red star. (C) Footprints of RapidEye imagery (© www.planet.com) with acquisition dates used in the present study. Grey rectangles delineate grid subsets created for feature tracking. Background in (A) and (C) from TanDEM-X digital elevation data (© DLR 2017).

2007, close to the Morenas Coloradas ice-debris complex (Trombotto Liaudat et al., 2020).

Given its proximity to the city of Mendoza, the Cordón del Plata has been the subject of numerous studies on periglacial landforms. Field studies are, however, limited to a few accessible locations on the eastern margin of the mountain range. Earlier studies mainly focused on the Morenas Coloradas complex and reveal the presence of permafrost down to ~3600 m a.s.l. (Barsch and King, 1989; Trombotto and Borzotta, 2009; Trombotto Liaudat et al., 2020) and indicate ongoing active surface deformation of ~2 m year^{-1} (Trombotto-Liaudat and Bottegal, 2019). Comparable results on the lower limit of discontinuous permafrost have been reported for the El Salto and Lagunita del Plata rock glaciers (Barsch and King, 1989; Trombotto et al., 1997), both similarly located on the eastern flank of the Cordón del Plata.

Methods

For the present study, we derived horizontal displacement rates of rock glaciers and ice-debris complexes from optical imagery for (a) 481 landforms contained in the ING for the Cordón del Plata range (Figure 1, Table 2) between 2010 and 2017/18 and (b) two local field sites for validation between 2017/18 and 2018/19. We further extract a variety of morphometric and topoclimatic metrics (Table 3) from a 12 × 12 m resolution TanDEM-X digital elevation model (DEM; © DLR 2017) for individual landform polygons to identify controlling variables on the landform's state of activity. Moreover, we seek to pinpoint local controls on surface kinematics by breaking down rock glacier and ice-debris complex polygons into a set of landform segments, oriented orthogonal to their flowline.

Inventory data for the Cordón del Plata

For the Cordón del Plata, the ING contains 1222 landform polygons that cover a total surface area of 251.71 km^2 (Table 2). Detailed information on the inventory for the three river basins that drain the Cordón del Plata can be found in accompanying reports (IANIGLA, 2018a,b,c). From this data set we exclude glaciers, debris-covered glaciers and permanent snow patches, and set a minimum threshold planimetric area of 0.025 km^2 for our analysis, leaving us with a total of 481 landforms that cover a surface area of 134.41 km^2. We further combine active and inactive rock glaciers into a single class of intact rock glaciers (Table 2), to avoid the inclusion of potential misclassifications owing to the subjective nature of visual interpretation of remotely sensed imagery.

We note here that the distinction between intact rock glaciers and ice-debris complexes throughout this paper is based on the

ING classification. Furthermore, the landform outlines were used as published by the ING; it is beyond the scope of our study to evaluate, let alone revise, mapped polygons.

Regional satellite imagery

For tracking the surface velocities of rock glaciers and ice-debris landforms in the Cordón del Plata range, we relied on optical RapidEye imagery that offers a reasonable compromise between spatial ground resolution and time span of availability. The RapidEye constellation consists of five identical satellites that collect data in five spectral bands with 6.5 m nominal ground sampling distance (Team Planet, 2018). To minimize the effects of snow and cloud cover, we aimed for images acquired at closely matching dates towards the end of the austral summer when weather conditions in the Andes cater for cloud-free conditions. As surface displacement of rock glaciers and ice-debris landforms is not expected to exceed several metres per year, we aimed to maximize the time span between the two images, to ensure large enough displacement between start and end images (Trombotto-Liaudat and Bottegal, 2019; Halla et al., 2020).

Given its size, no images were available that cover the full study area. Therefore, a set of two scenes was selected for both the northern and southern part of our study area (Figure 1). We used images acquired by RapidEye1 satellite on 2010-03-16 and 2018-03-17 in the northern and by RapidEye5 satellite on 2010-03-10 and 2017-04-13 in the southern study region, respectively. We favour RapidEye Level 3A products that are sensor-corrected, orthorectified using ground control points and with 30–90 m resolution SRTM DEMs, resampled to 5 × 5 m ground resolution (Team Planet, 2018) over RapidEye Level 1B products that we orthorectified using a TanDEM-X DEM with 12 × 12 m ground resolution. Though both products yield very similar results, large data gaps and errors in the TanDEM-X, especially along ridge crests (see Figure S1) but also touching the position of rock glaciers in valley floors, introduce uncertainties that might impair the quality of our analysis.

Field-site-specific structure from motion photogrammetry

To validate the surface displacement results generated from optical satellite imagery, we obtained DEMs and orthoimages from aerial photography collected with an unmanned aerial vehicle (UAV) for the Morenas Coloradas and Stepanek ice-debris complexes, located in the northeastern part of our study region (Figure 1). The Morenas Coloradas ice-debris complex was surveyed at the end of the ablation season in 2017 and 2018, using a Phantom 3 Advanced

Table 2. Landform types, numbers and areas as contained in the national glacier inventory (ING) for the Cordón del Plata (IANIGLA, 2018a, 2018b, 2018c)

| | National glacier inventory | | This study (min. area 0.025 km^2) | |
Landform	Number	Area (km^2)	Number	Area (km^2)
Glaciers	287	92.87	excluded	
Debris-covered glaciers	57	11.62	excluded	
Ice-debris complexes	81	72.93	77	72.90
Active rock glaciers	438	58.37		
Inactive rock glaciers	37	4.37	404	61.51
Permanent snow patches	322	11.55	excluded	
Total	**1222**	**251.71**	**481**	**134.41**

Table 3. Morphometric and topoclimatic variables calculated for landform polygons and segments

Variable (unit)	Statistics used	
	Landform (abbreviation)	Landform segment (abbreviation)
Area (m^2)	Planimetric area (A$_{LF}$)	Not meaningful
Width (m)	Mean width perpendicular to centreline (W$_{LF}$)	Width perpendicular to centreline (W$_{SG}$)
Length (m)	Landform length along flowline (L$_{LF}$)	Length position along flowline (L$_{SG}$)
Elevation (m)	Min, max, mean, range (Z$_{min}$, Z$_{max}$, Z$_{mean}$, Z$_{range}$)	Mean (Z$_{mean}$)
Slope (°)	Min, max, mean, IQR (S$_{min}$, S$_{max}$, S$_{mean}$, S$_{range}$)	Mean (S$_{mean}$); see Figure 2
N-exposedness (–)	Cosine of mean aspect (N$_{exp}$)	Cosine of mean aspect (N$_{exp}$)
E-exposedness (–)	Sine of mean aspect (E$_{exp}$)	Sine of mean aspect (E$_{exp}$)
Potential incoming solar radiation (PISR) (kWh m^{-2} a^{-1})	Min, max, mean, IQR (PISR$_{min}$, PISR$_{max}$, PISR$_{mean}$, PISR$_{IQR}$)	Min, max, mean, IQR (PISR$_{min}$, PISR$_{max}$, PISR$_{mean}$, PISR$_{IQR}$)
Feeder basin area (m^2)[†]	Catchment area feeding into the landform (FBA$_{LF}$)	Catchment area feeding into the segment (FBA$_{SG}$)
Basin elevation range (m)[‡]	Headwall to toe elevation range (HTTE)	Headwall to segment elevation range (HTSE)
Angle of reach (°)[‡]	Angle between highest point of headwall and lowest point of toe along the centreline (AOR$_{LF}$)	Angle between highest point of headwall and mean segment elevation along the centreline (AOR$_{SG}$)
Geometric slope (°)[‡]	Angle between highest point of headwall and lowest point of toe along Euclidean distance (GS$_{LF}$)	Angle between highest point of headwall and mean segment elevation along Euclidean distance (GS$_{SG}$)
Average slope (°)	Angle between highest point of landform and lowest point of toe along Euclidean distance (AS$_{LF}$)	Not meaningful
Headwall area (m^2)[§]	Slope-adjusted area with inclination of >25° above the landform (HWA$_{LF}$)	Slope-adjusted area with inclination of >25° above the segment (HWA$_{SG}$)
Headwall height (m)	Highest point of headwall to highest point of landform (HHW)	Not meaningful
Topographic wetness index (–)	99th percentile ln(A/tan(slope)) (TWI)	Not meaningful

[†]Feeder basins were derived using all pixels above the 25th elevation percentile as pour points, to avoid overestimation by trunk-valley inclusion. For the landform compartments, feeder basins were derived using all pixels as pour points; to assure growing basin size approaching the toe positions, the contributing area was cumulated over upslope compartments. Owing to the poor quality of TanDEM-X data along the ridges (Figure S1), we rely on 30 × 30 m ground resolution SRTM DEMs for the calculation of feeder basins.

[‡]Just valid for landform segments along the main branch of the landform. For modelling, segments along tributary branches ($n = 141$, ~10% of total segments) are therefore excluded.

[§]Headwall size is defined here as the slope-corrected surface area of all feeder basin pixels with slopes larger than 25°.

multicopter equipped with a standard camera (12.4 MP, FOV 94°), taking ~3900 and ~2000 overlapping images, respectively. Due to the large survey area (>2 km^2), flights were conducted during multiple days (06/02 to 18/02/2017 and 16/02 to 22/02/2018), depending on weather conditions. Across the ice-debris complex and stable bedrock outcrops in its vicinity, we distributed 55 ground control points (GCPs) that were measured with a Trimble R8s/R2 differential global navigation satellite system (dGNSS) operating in a real-time kinematic base-rover configuration. The GCP positions have horizontal and vertical mean accuracies of 0.010 and 0.020 m for 2017, and 0.011 and 0.020 m for 2018, respectively. GCPs were distributed over the survey area as reference points for the UAV survey and as direct measurements of surface displacement. Five GCPs were located on stable bedrock outcrops outside the moving RG area. On the Stepanek ice-debris complex, flight campaigns with the same equipment were realized during the end of the austral summers of 2018 (08/02 and 09/02; ~850 images) and 2019 (15/03; ~1300 images). Here, 31 GCPs were measured with horizontal and vertical mean accuracies of 0.009 and 0.020 m for 2018 and 0.006 0.010 m for 2019, respectively, nine of which were located on stable surfaces.

Using structure from motion multi-view stereo algorithms, we constructed dense point clouds using AgisoftPhotoscan Professional (Version 1.4.4) with high-quality and moderate depth filtering. As orthoimages collected in consecutive years show large spectral differences, due to shadowing effects, snow cover, surface moisture, etc., DEMs and their derivatives have proven an adequate surrogate input for image cross-correlation applications (Dall'Asta *et al.*, 2017).

Feature tracking

The analysis of horizontal displacement rates of periglacial landforms is widely applied to objectively assess a rock glacier's state of activity. Furthermore, detailed 2D motion fields reveal spatial variability of rock glacier kinematics and help to gain further insight into rock glacier movement (Kääb and Vollmer, 2000; Bodin *et al.*, 2018). Different techniques for monitoring rock glacier creep are available, amongst them direct field measurements such as repeated geodetic field surveys (Krainer and Mostler, 2006; Scapozza *et al.*, 2014) and the installation of GNSS loggers (Wirz *et al.*, 2016). To obtain a better spatial coverage of surface displacement, remote-sensing techniques like airborne and terrestrial laser scanning (Bodin *et al.*, 2018; Kummert and Delaloye, 2018), differential synthetic aperture radar interferometry (DInSAR; Villarroel *et al.*, 2018; Strozzi *et al.*, 2020), and the manual or automated tracking of features in oriented aerial or terrestrial imagery (Kääb and Vollmer, 2000; Scapozza *et al.*, 2014; Groh and Blöthe, 2019) have been used widely. Recently, the advancement of photogrammetric software solutions has spurred periglacial research using UAV-derived imagery for the production of high-resolution DEMs and orthoimages (Dall'Asta *et al.*, 2017; Vivero and Lambiel, 2019).

Here we apply a least-squares matching (LSM) algorithm as implemented in Environmental Motion Tracking software (EMT Version 9.1, http://www.tu-dresden.de/geo/emt; Schwalbe and Maas, 2017) to automatically track features and derive horizontal surface displacement of rock glaciers and ice-debris complexes in the Cordón del Plata ranges. EMT software applies an area-based matching strategy to automatically identify corre-

sponding patches of pixel values in multi-temporal images using LSM or cross-correlation algorithms (Förstner, 1986; Schwalbe and Maas, 2017). Sequential images are loaded into EMT software, where object points (patch centres) are defined, patch size and search area are set, and tracking method as well as master and slave image are selected. While the patch size indicates the area of image values to match between images, the search area defines the maximum offset of the patch between master and slave image. Tracking is done in a two-stage operation in which cross-correlation is used for rough pixel-precise matching in a first step, followed by iterative LSM that achieves subpixel accuracies in a second step (see Schwalbe and Maas, 2017 for details).

For the regional analysis of the present study, we applied a LSM approach with shadow removal to sequential RapidEye image pairs with a 5×5 m ground resolution. To reduce computational requirements, we subdivided the study area into 28 rectangular subsets of 8×8 km (Figure 1C). Within each subset, object points for feature tracking were evenly spaced based on a 10×10 m grid within a 50 m buffer of the ING polygons. We tracked object points using three different rectangular patch sizes varying between 15, 20 and 30 pixel edge lengths and a fixed search area of 15×15 pixels. Trajectories were only calculated for object points with correlation coefficients larger than 0.75 and which could be successfully calculated by LSM. Following Groh and Blöthe (2019), we further exclude trajectories that deviate more than 45° from the mean bearing of their 3×3 neighbours as well as from the topographic aspect as derived from a TanDEM-X DEM to avoid the inclusion of erroneously matched image patches. In a final step, filtered tracking results for different patch sizes were averaged, rasterized to a 10×10 m grid, and clipped to the ING polygon boundaries. For the two field sites of Morenas Coloradas and Stepanek, object points for feature tracking were evenly spaced in a 10×10 pixel grid on a 0.5×0.5 m resolution UAV-derived DEM. Tracking was done on hillshade images using a patch size and search area of 30 pixels edge length; filters were applied as described above.

To account for systematic positional offsets between image pairs, EMT offers the possibility to track fix points (i.e. stable surfaces outside moving features). Apparent fix-point offsets serve to calculate affine transformation parameters between image pairs and to correct final object-point trajectories. Here we created a set of 2000 fix points located on stable areas outside ING inventory polygons for each image subset to correct tracking results for potential systematic image mismatches. On average, >60% of fix points were successfully tracked and used to determine the affine transformation for each 8×8 km subset of RapidEye imagery (Table S1). For the UAV data from the two field sites, fix-point tracking was deemed unnecessary, as both sets of images were directly referenced using dGNSS GCPs.

However, despite affine transformation or direct georeferencing using GCPs, residual positional errors and errors associated with LSM matching potentially compromise tracking results. To avoid the inclusion of spurious displacement values, we calculate a minimum level of detection (LoD) that determines a threshold to discriminate significant changes from non-significant noise. Following earlier studies that apply feature tracking to optical imagery (e.g. Luckman *et al.*, 2007; Liu *et al.*, 2020), we track an independent set of 2000 object points on stable surfaces and estimate the LoD using:

$$\text{LoD} = t*\text{stdv}*\sqrt{d_x^2 + d_y^2} \qquad (1)$$

where t is the factor for given confidence intervals and degrees of freedom in a Student's t-distribution, stdv is standard deviation, and d_x and d_y are the differences in x and y coordinates between RapidEye and UAV-derived image pairs. All trajectories that fall below the minimum LoD are masked out and considered insignificant. Analogously, we use Equation 1 to calculate the minimum LoD for the measurement of surface displacement from dGNSS surveys, using the spurious displacement d_x and d_y between repeatedly measured fix points in the field.

Centrelines and landform segments

We adopt the approach presented by Kienholz *et al.* (2014) and derive centrelines for all rock glaciers and ice-debris complexes based on a least-cost route approach. The algorithm is fully automated and relies solely on a DEM and mapped landform outlines to extract the termini and valley heads for all landforms in a first step. Based on the observation that glaciers (and other ice-containing landforms) flow under the force of gravity and that flow tends to be faster in the centre (Haeberli, 1985), the least-cost path estimate is based on a penalty grid value (p_i) that combines distance to the landform's outline and the elevation:

$$p_i = \left(\frac{\max(d) - d_i}{\max(d)}*f_1\right)^a + \left(\frac{z_i - \min(z)}{\max(z) - \min(z)}*f_2\right)^b \qquad (2)$$

where d_i and z_i are the Euclidean distance of a cell i from the edge of the landform's polygon and z_i is the elevation of that cell, respectively. Coefficients f_1 and f_2 and exponents a and b are empirical parameters for which we used proposed values of $f_1 = 1000$, $f_2 = 3000$, $a = 4.25$, $b = 3.6$ (see Kienholz *et al.*, 2014 for details). Subsequently, the least-cost route from a given source point to the lowest point at the landform's terminus is determined by finding the path with minimum accumulated penalty values p_i. In a final step, centrelines are smoothed, split into branches and ranked according to their length (Figure 2). For further analysis of longitudinal variability of surface displacement, we constructed rectangular segments oriented perpendicular to the centrelines with a maximum width of 500 m and a constant length of 150 m in the direction of flow (Figure 2) (i.e. with a maximum surface area of 0.075 km^2, containing a maximum of 750 tracked pixels). Compartments were clipped by the landform polygon and used to extract topoclimatic and morphometric parameters (Table 3).

Candidate predictor variables

In the absence of rigorous climatic data in the region, we rely on topoclimatic and morphometric parameters instead to identify potential controls on the state of activity of entire landforms and individual segments of these. For all rock glacier and ice-debris complex polygons, their landform segments and feeder basins, defined here as the upslope contributing area delivering water (solid and/or liquid) and debris to the landform, we extracted candidate predictors (Table 3). Key topoclimatic parameters, such as elevation, slope, aspect, potential incoming solar radiation (PISR) and their derivatives, were derived from a TanDEM-X DEM, while geometric predictors, amongst them planimetric area of landform and feeder basin, as well as the dimensions and average inclinations, were derived using mapped polygons from the ING in combination with the DEM (see Table 3 for details).
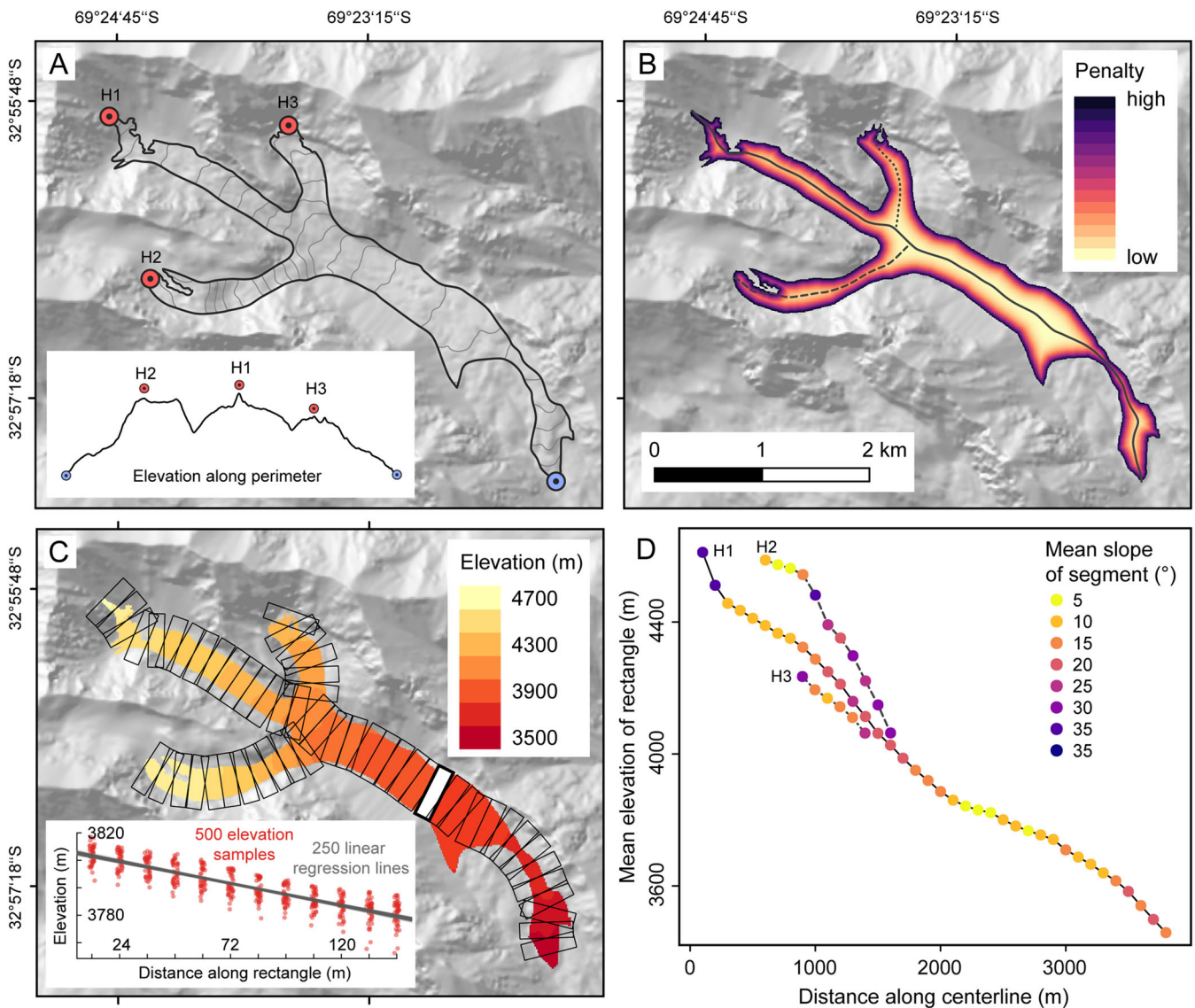
Figure 2. Automated extraction of centrelines from TanDEM-X topographic data for the Morenas Coloradas ice-debris complex in the Argentinian Andes. (A) Identification of valley heads (H1–H3, red points) and the lowest point (blue point) by finding peaks and the absolute minimum of elevation values along the mapped landform outline (inset). (B) Smoothed centrelines from a least-cost route analysis of a penalty grid combining the distance to the nearest border and the absolute elevation of the landform (see Kienholz et al., 2014 for details). (C) Perpendicular rectangles of 150 m length (in direction of flow) and 500 m width. Mean slope is calculated by fitting 250 linear regression models to repeated samples of 500 elevation values within each rectangle (inset). (D) Long profile for three centrelines extracted for the Morenas Coloradas ice-debris complex, colour-coded by the mean slope of each rectangle. Background in (A)–(C) from TanDEM-X digital elevation data (© DLR 2017).

Random forest classification

In a final step, we model the activity state of (a) entire landform polygons and (b) landform segments of rock glaciers and ice-debris complexes in the Cordón del Plata ranges. Modelling rock glacier activity as a binary variable can be achieved with a variety of different approaches. In the context of studies predicting rock glacier activity, logistic regression models enjoy great popularity (Brenning and Trombotto, 2006; Brenning and Azócar, 2010), but recently machine learning techniques such as support vector machines and random forests have proven their applicability to the rock glacier context (Groh and Blöthe, 2019; Kofler et al., 2020). Here we implement a random forest classification algorithm, given the predictive performance and the straightforward estimates of feature importance.

Random forest classification, introduced by Breiman (2001), is a machine learning technique that combines a large number of individual decision trees to an ensemble model. Classification trees are grown using recursive binary splitting on a random subset of the training data. To avoid correlation of individual trees, variables are drawn from a randomly selected predictor subset at each split. This approach allows quantifying the importance of each variable that can be expressed as the mean decrease in classification accuracy when a given predictor is excluded from the model (Breiman, 2001; James et al., 2013). To avoid biased model results due to spatial correlation, we favour repeated leave-location-out cross-validation (LLO-CV; spatial k-fold cross-validation) over spatially inexplicit sampling of training and test sets (Meyer et al., 2018). Using a k-means clustering algorithm, our study area was subdivided into five regions and we repeated LLO-CV 25 times for each region (i.e. 125 model runs for each model). LLO-CV models are trained on random subsamples that are drawn from four of the five spatial clusters, while testing the performance of the models is achieved on the fifth region (Brenning et al., 2012; Meyer et al., 2018).

For both modelling the activity of entire landforms and of landform segments, two different parameter sets were tested. We compared the performance of random forest models using the full parameter set with the performance of a model that

iteratively increases the number of parameters used in a forward feature selection (FFS) approach (Meyer *et al.*, 2018).

Random forests were grown using the R package *caret* (Kuhn, 2008) that serves as a wrapper for the *RandomForest* R package (Liaw and Wiener, 2002), while FFS and LLO-CV were performed using the R package *CAST* (Meyer *et al.*, 2018). We set the number of trees grown for each model to 500 (*ntrees*) and tested the performance of the hyperparameter *mtry* (i.e. the number of variables tested at each split, for values between 2 and 9 for the full and reduced parameter set).

Results

Local variability of surface displacement

Using a set of two cloud-free RapidEye images for the northern and southern parts of the Cordón del Plata (Figure 1), respectively, we set out to automatically track the surface movement for 481 rock glaciers and ice-debris complexes contained in the ING. After data filtering and clipping of the results to the inventory polygons, we excluded 186 landforms from all further analysis, for which less than 100 pixels (10^4 m^2) or a minimum of 20% of the surface area could be successfully tracked, leaving us with 295 landforms that cover a surface area of 101.85 km^2 (Table 4). Image mismatches due to changing local conditions and errors associated with georeferencing and orthorectification procedure influence the minimum LoD that varies depending on location. For 23 out of 28 subregions used for tracking (Figure 1), LoD ranges between 0.28 and 0.55 m year^{-1}, while for five subregions in the southeast LoD exceeds 0.8 m year^{-1} (Figure S1, Table S1).

Tracking the horizontal displacement of rock glaciers and ice-debris landforms in our study area successfully depicts heterogeneous velocity fields of individual landforms (Figure 3). While some examples show rather uniform advancement across their full width (Figure 3C), displacement is focused in narrow belts of rapid movement (Figures 3A and B) or mirrors the compound nature of individual landforms contained in the inventory (Figure 3D). Besides the lateral variability with focused deformation in the central part, displacement also varies greatly longitudinally.

Adapting a straightforward morphometric approach (Kienholz *et al.*, 2014), we derived centrelines for 295 rock glaciers and ice-debris complexes and constructed more than 2500 perpendicular landform segments, 1383 of which cover an area >0.01 km^2 and have >50% of their surface successfully tracked. Segments were used to extract velocity distributions, mean elevation and mean slope (Figure 2) to (i) construct longitudinal profiles for selected landforms (Figure 4) and (ii) investigate controlling variables on the local state of activity. Velocity distributions along the centrelines of main and tributary stems highlight the large variability of displacement within single landforms. Rates exceeding 3.0 m year^{-1} are common for landforms in the Cordón del Plata and are attained not only in the upper and middle parts, but also occur frequently towards their frontal positions (Figures 3 and 4). For selected profiles our data shows a close association between surface velocities and local slope along the centreline (Figures 4A, B and D), with higher inclination corresponding to higher surface velocity. However, we also find opposite examples where an acceleration is rather associated with decreasing slope angles (Figure 4C), again emphasizing the large heterogeneity found in the kinematics of a large number of rock glaciers and ice-debris landforms. This is further reflected by the full set of 1383 segments, for which we find significant positive trends for median velocity against mean slope for the 10th and 25th percentile using quantile regression, though the increase in median velocity per unit surface slope remains below 1 cm.

Comparison with ground truthing from local field sites

During repeated field stays in the austral summers of 2017, 2018 and 2019, we collected independent measurements of surface displacement of two landforms in the Cordón del Plata range, the Morenas Coloradas (2.38 km^2) and Stepanek (0.73 km^2) ice-debris complexes, to validate the tracking results derived from RapidEye satellite imagery. Given their large extent, the field surveys focused on the lower parts of these landforms. For both Morenas Coloradas and Stepanek, repeated dGNSS measurement of GCPs located on individual boulders and bedrock outcrops indicates horizontal displacements of >3.0 and >1.5 m year^{-1}, respectively (Figures 5 and S3). Using EMT, automated feature tracking on high-resolution hillshades yielded reliable 2D velocity fields for the lower parts of Morenas Coloradas and Stepanek, with LoDs of 0.52 and 0.24 m year^{-1}, respectively (Figures 5 and S3). The Morenas Coloradas rock glacier shows high surface speeds in the upper part of the area covered, exceeding 3 m year^{-1} along its central flowline, before generally slowing down in the middle section where movement gets funnelled and surface speeds increase towards the toe, again exceeding 3 m year^{-1} close to the terminus (Figure 5B). In contrast, the surveyed part of the Stepanek rock glacier generally moves slower and surface velocities constantly drop towards the snout, where displacement falls below the LoD of the feature-tracking approach and is only detectable by dGNSS measurements (LoD 0.08 m year^{-1}; Figure S3).

Comparison of the surface velocities derived from dGNSS and feature tracking in UAV-derived hillshades allows us to assess the accuracy of deriving velocity fields from RapidEye remote-sensing imagery. Qualitatively, the spatial pattern of the RapidEye tracking velocities closely matches the 2D velocity fields computed from UAV-derived DEMs for both field sites (Figures 5 and S3). Moreover, mean absolute errors between RapidEye-derived surface motion and in-field dGNSS measurements are 0.306 and 0.270 m year^{-1}, respectively, roughly corresponding to LoDs determined from stable surface displacements in RapidEye imagery. We are therefore confident that tracking horizontal displacement in remote areas of the

Table 4. Periglacial landforms grouped according to whether or not their displacement surpasses the level of detection of our analysis

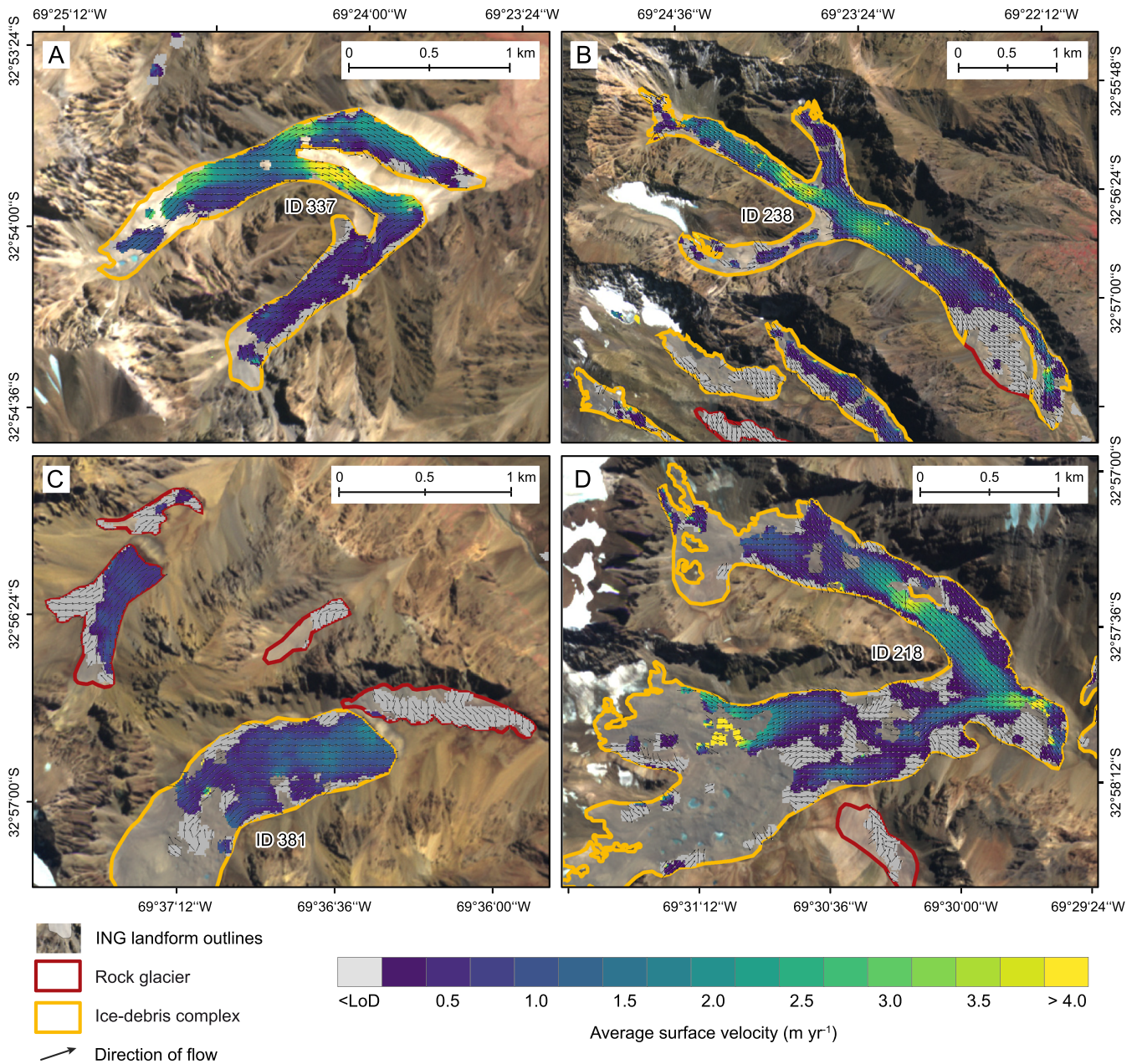| Landform	Displacement larger than LoD		Displacement smaller than LoD	
	Number	Area (km^2)	Number	Area (km^2)
Ice-debris complexes	34	38.15	17	19.57
Intact rock glaciers	115	24.26	129	19.87
Total	**149**	**62.41**	**146**	**39.44**

Figure 3. Examples of average surface displacement between 2010 and 2018 for rock glaciers and ice-debris complexes in the Cordón del Plata range. Colours with superimposed arrows show displacement larger than LoD, grey colours with arrows indicate tracked cells with non-significant movement. Transparent grey polygons with red and orange outline show rock glacier and ice-debris complex polygons as contained in the ING, respectively. IDs given for landforms shown in Figure 4. Background RapidEye imagery in (A)–(D) from www.planet.com.

Cordón del Plata region using RapidEye satellite imagery yields reliable estimates of rock glacier and ice-debris complex surface velocities.

Regional distribution of active landforms

For 149 successfully tracked landforms, we find surface displacement exceeding the LoD of our analysis (i.e. with active movement), while for the remaining 146 landforms, tracked pixels show displacement values below the LoD (Table 4). Following this binary classification, actively moving landforms account for ~60% of the area successfully tracked, while the remaining ~40% show no significant movement with respect to the LoD. On average, owing to their compound nature, ice-debris complexes are larger than rock glaciers and show higher rates of displacement (Figure 6). Using quantile regression, mean surface velocities of actively moving landforms show significant positive correlations (99% confidence interval) to planimetric area, with slopes ranging between 0.24 and 0.36 m year^{-1} km^{-2} for the 25th, 50th and 75th percentiles (Figure 6). However, these trends are insignificant if looking at intact rock glaciers ($n = 115$) and ice-debris complexes ($n = 34$) separately. Overall, median surface velocities of actively moving rock glaciers and ice-debris complexes in the Cordón del Plata range vary between 0.35 and 1.79 m year^{-1} (Table S2).

The regional distribution of active rock glaciers and ice-debris complexes (i.e. displacement larger LoD) is heterogeneous. Regarding the maximum velocities of active landforms, taken here as the 95th percentile of the distribution to avoid overestimation due to isolated values, the central and eastern part of the Cordón del Plata range seem to feature higher displacements compared to the northern and southern parts of the study area. While the 95th percentile of surface velocities for the majority (129 out of 149) of tracked landforms
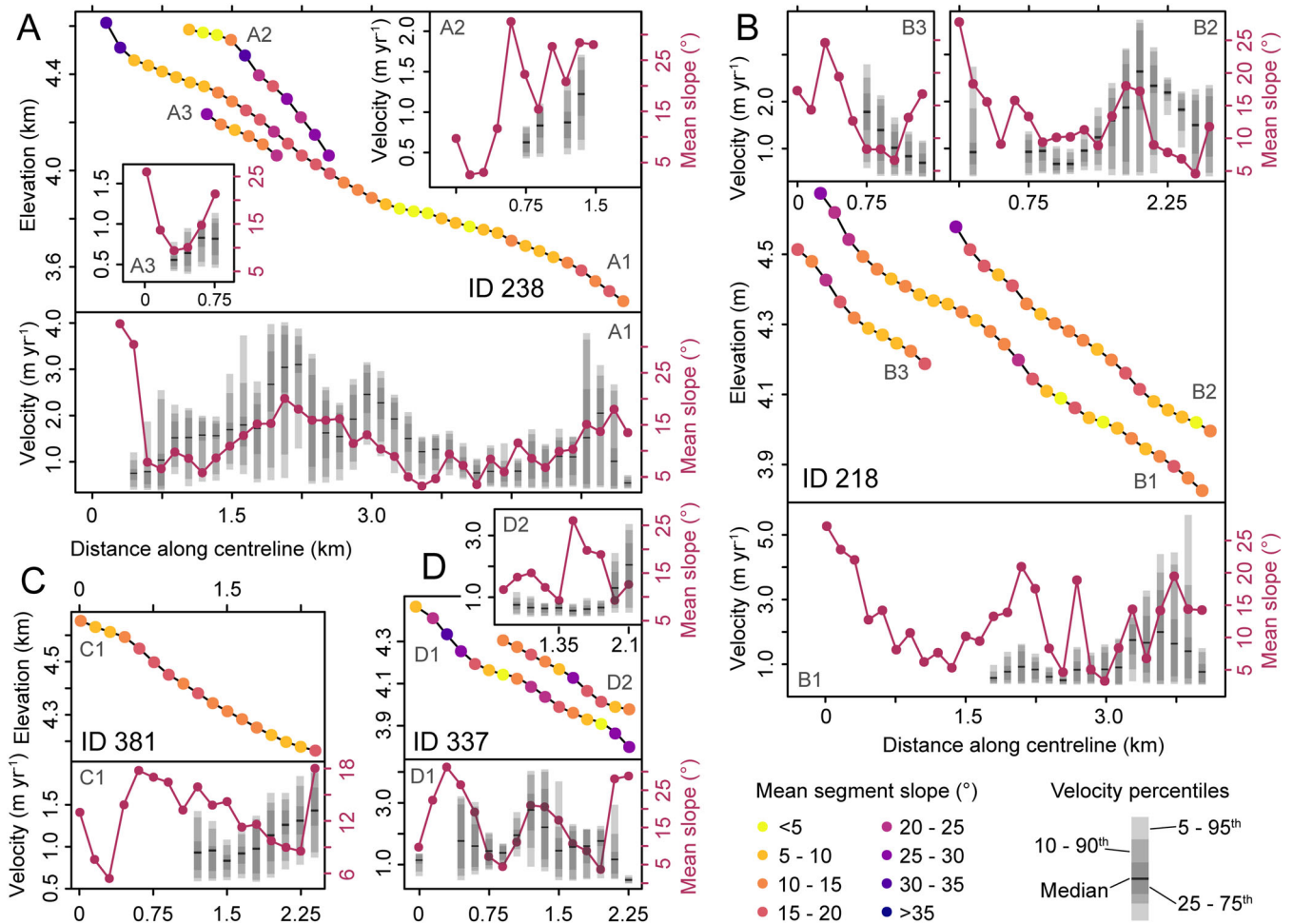
Figure 4. Longitudinal profiles from landform segments for rock glaciers and ice-debris complexes. Profiles are colour-coded to the mean slope of the segments; insets show mean slope (red) and percentiles of RapidEye-derived velocity distribution (grey bars). See Figure 3 for location of landforms shown here.

remains below 3 m year^{-1}, it exceeds speeds of 3.5 m year^{-1} for 14 examples (Figure 7A, Table S2). Owing to varying snow cover and shadowing effects in the RapidEye images used for the southern part of the study area, however, fewer landforms with overall higher LoDs could be tracked successfully compared to the northern part (Figures 7A and S2, Table S2), potentially disguising activity in these areas.

Vertically, a clear stacking of actively moving versus stagnant inactive landforms is not apparent; both are present in nearly all elevation bands. Maximum values of 95th percentile velocities (i.e. exceeding 3.5 m year^{-1}) are only found above a mean elevation of 4100 m a.s.l. Overall, 95th percentile velocities between LoD and 2 m year^{-1} predominate in all elevation bins, except between 4400 and 4500 m a.s.l. where the distribution is more balanced. Between 4100 and 4500 m a.s.l., rock glaciers and ice-debris landforms seem to find optimal conditions; more than 60% of landforms are located here, covering nearly two-thirds of the total areal extent (Figure 7B).

Predicting state of activity and identifying morphometric controls

We modelled the state of activity of (a) entire landform polygons and (b) landform segments of rock glaciers and ice-debris complexes as a binary categorical variable using a random forest classification approach. We acknowledge here that, based on our data, we cannot determine the state of

activity unambiguously. Yet, the velocity fields generated in this study allow us to define two distinct groups of landforms and landform segments: class 1 contains features with surface displacement exceeding the LoD of our analysis; class 0 contains features that show movement which remains below the LoD. To reduce potential bias from largely different LoD values that separate these two classes, we only include features with LoD values ranging from 0.28 to 0.55 m year^{-1} in our model, reducing the set of 295 landforms to 135 in class 1 and 109 in class 0, respectively. From the total of 1383 successfully tracked landform segments, we assigned those to class 1 that have mean velocities exceeding the LoD, while the remainder with mean velocities below the LoD were assigned to class 0. For modelling, we analogously exclude data with LoD > 0.55 m year^{-1} and focus on segments along the main stem only, resulting in 659 segments in class 1 and 361 segments in class 0.

Using a subset of eight predictor variables, we can predict the state of activity of rock glacier and ice-debris landform polygons in the Cordón del Plata rage with an overall accuracy of 70.08% [mean area under receiver operator characteristic curves (AUROC) = 0.785]. Using the full parameter set of 25 predictors, we achieve slightly lower overall accuracy (69.67%) and mean AUROC (0.743) values (Figure 8). Fivefold LLO-CV indicates good transferability of the individual folds of the model in four out of five regions (AUROC between 0.743 and 0.878). Prediction in region #5, however, yields consistently lower AUROC values for LLO-CV of 0.656 and 0.633 for the full and reduced parameter set, respectively (Figure 8).
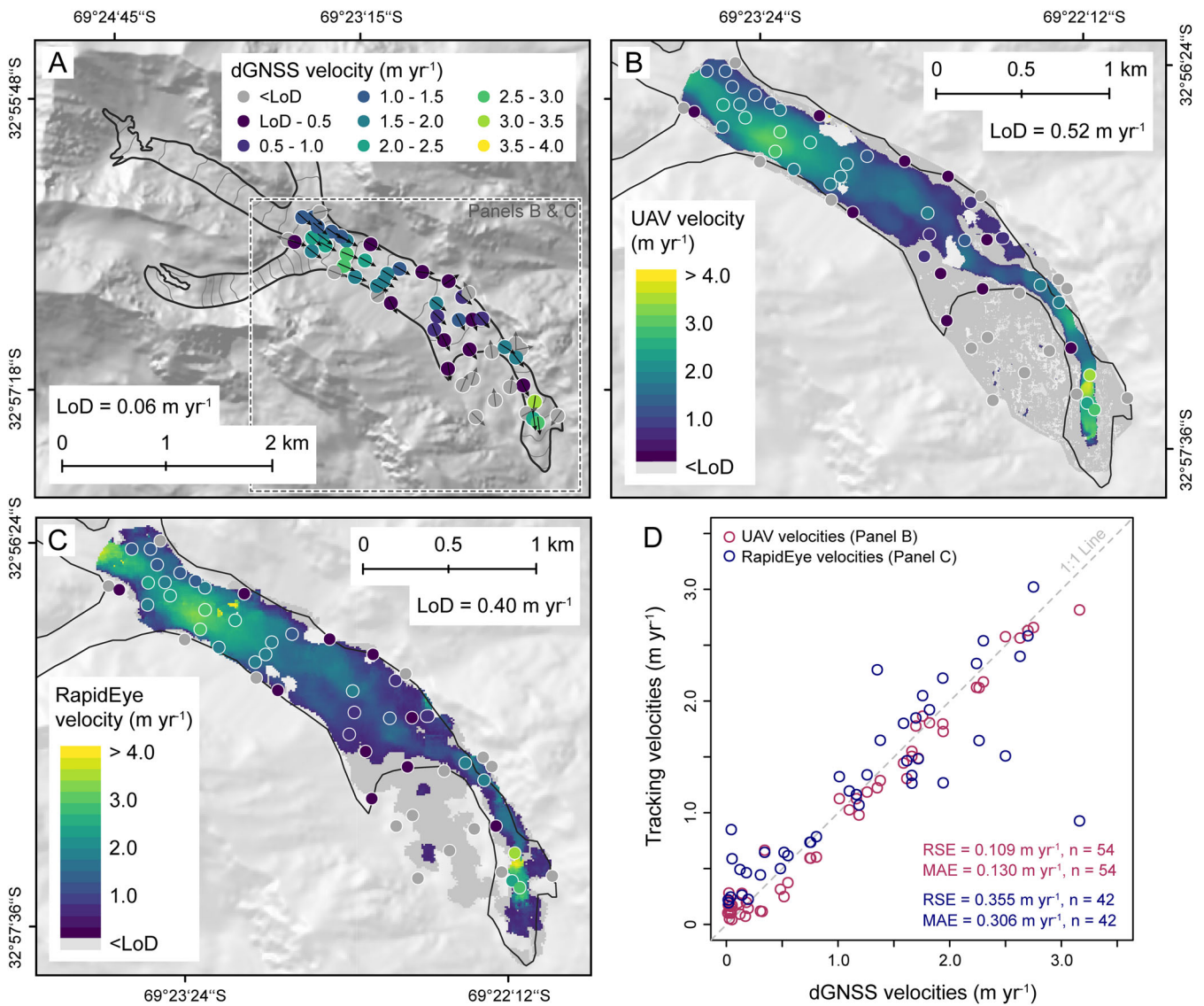
Figure 5. Horizontal surface displacement of the Morenas Coloradas ice-debris complex, as determined by (A) repeated dGNSS surveys of 55 ground control points in 2017 and 2018; (B) feature tracking of repeated UAV-derived digital elevation models in 2017 and 2018; and (c) feature tracking in RapidEye satellite imagery from 2010 and 2018. (d) Comparison between dGNSS-measured velocities for 2017/18 and the velocities estimated by feature tracking in UAV-derived elevation data for 2017/18 (red) and RapidEye imagery for 2010/18 (blue), respectively. For both, residual standard error (RSE) and mean absolute error (MAE) are given to quantify deviation from the 1:1 line.

For both models, using the full parameter set and a reduced FFS parameter set, minimum PISR ranks as the second most important variable for distinguishing between landforms with horizontal displacement values above and below the LoD (Figure 9). For the reduced parameter set, PISR is preceded by the size of the headwall, and followed by the landforms' geometric slope. For the full parameter set, the landforms' elevation range ranks most important, with headwall size and headwall to toe elevation range, further PISR statistics and topographic wetness index following minimum PISR. Furthermore, the landforms' average slope, feeder basin area and length of landform rank in the top ten.

On the smaller scale of the landform segments, predicting the state of activity with random forest models performs equally well. Running models with fivefold LLO-CV and 25 repetitions, we can predict the state of activity of landform segments with an overall accuracy of 74.00% (mean AUROC = 0.714) and 74.86% (mean AUROC = 0.753), based on the full parameter set and a reduced parameter set using FFS, respectively. Here, fivefold LLO-CV indicates reasonable transferability of the models, with four test regions yielding comparable results for the full parameter set, while predicting activity in regions #3

and #5 with the reduced parameter set performs significantly less well than the mean model (Figure 10).

For both parameter sets the angle of reach shows the highest variable importance for predicting the state of activity of landform segments on the local scale. Furthermore, the length position along the centreline, the feeder basin area and minimum PISR rank among the five most important variables for both classifications (Figure 11).

Discussion

Horizontal velocities and state of activity in the Cordón del Plata range

Applying a feature-tracking algorithm to repeated RapidEye satellite images, we can objectively quantify the velocity fields of 244 rock glaciers and 51 ice-debris complexes in the Cordón del Plata range of the Central Andes of Argentina. Optical feature tracking proves most applicable to rather smooth surfaces, while changing snow cover, shadowing effects and the
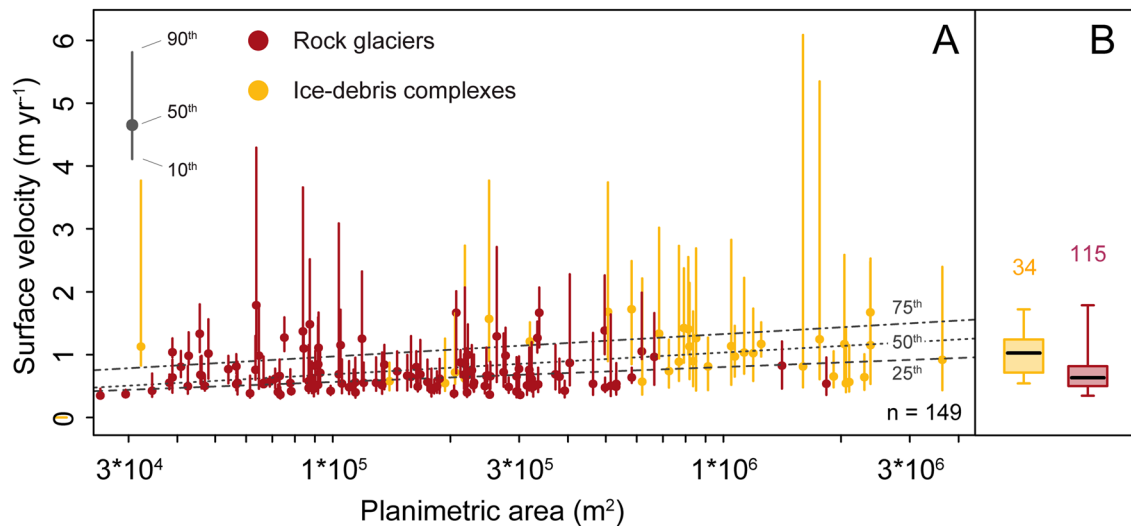
Figure 6. Average surface displacement for 149 rock glaciers and ice-debris complexes in the Cordón del Plata range between 2010 and 2017/18. (A) Displacement vs. planimetric area, colour-coded by landform type. Points indicate median velocities, whiskers show 10th to 90th percentiles. Dashed, dotted and dash-dotted lines depict significant quantile regression fits for the 25th, 50th and 75th percentiles. (B) Boxplots summarizing median velocities per landform type; whiskers extend to minimum and maximum values, numbers indicate sample size.

development of thermokarst lakes on the landform's surface hinders successful tracking (Figure 3) (Monnier and Kinnard, 2017). Furthermore, off-nadir angle correction during orthorectification produces stretched and clinched pixels, potentially influencing tracking reliability between images. However, as most features surveyed in our study have rather low surface inclinations, we regard this effect as a minor source of error. Comparison with two ground-truthing sites yields closely matching results in both magnitude and spatial pattern of surface displacement, with mean absolute errors between 0.27 and 0.31 m year^{-1}, suggesting our RapidEye-derived tracking data to be highly reliable. However, we note here that remote-sensing and ground-truthing data cover different time intervals: while satellite imagery spans the time from 2010 to 2018, ground truthing on Morenas Coloradas and Stepanek ice-debris complexes was conducted between 2017/18 and 2018/19, respectively. Still, we see no indication for drastically changing deformation patterns and take our closely matching rates obtained from different methods and timings as a sign of little interannual variability of surface deformation in the study region.

We find significant horizontal displacement for 115 rock glaciers and 34 ice-debris complexes, leaving 129 and 17 landforms, respectively, that show no significant movement with respect to the LoD of our analysis (Table 4). Based on visual interpretation of remotely sensed imagery, the ING classifies 234 of these 244 rock glaciers as actively moving, with no information given on the state of activity of ice-debris complexes (IANIGLA, 2018d). This large discrepancy underlines the potential benefit of objectively measuring surface displacement from remote-sensing imagery to investigate rock glacier activity (Strozzi *et al.*, 2020), and to update inventory data that is based on visual interpretation alone. Clearly, part of the ratio between objective quantification and visual interpretation might be owing to surface displacement that falls below the LoD of this study. However, differences of up to −74% between objective quantification and visual interpretation in the ING have been reported by Villarroel *et al.* (2018), who survey rock glacier activity in the Argentinian Andes using DinSAR, capable of resolving displacements of a few centimetres per year. In either case, the high percentage of active versus inactive landforms in the Central Andes is remarkable, attaining nearly 50% in our data if compared to values of

29–36% found in the Austrian Alps (Krainer and Ribis, 2012; Groh and Blöthe, 2019).

Detailed field studies on rock glacier and ice-debris complex kinematics that might serve as additional ground truth remain sparse in the Central Andes. For three ice-debris complexes and one rock glacier in the Central Chilean Andes, average velocities range from 0.5 to 1.1 m year^{-1} between 1955 and 2014 and 0.87 m year^{-1} between 2010 and 2012, respectively (Monnier and Kinnard, 2016, 2017). Though not in the direct vicinity, the mean displacement between 0.37 and 2.61 m year^{-1} found in this study encompasses the reported range, but points to systematically higher displacement values on the eastern side of the Andes, where 25% of the landforms have mean velocities exceeding 1.13 m year^{-1} (Table S2). Yet it must be noted that our data set contains 149 actively deforming landforms, perhaps better reflecting the complete portfolio of surface displacement magnitudes found in the Central Andes. Independent data for the Morenas Coloradas ice-debris complex confirm the heterogeneity of horizontal displacement, with values surpassing 2 m between May 2015 and February 2016 close to the frontal position and in the central upper parts, while lower rates dominate lateral positions (Figure 5) (Trombotto-Liaudat and Bottegal, 2019).

Systematic studies that survey and analyse the surface kinematics of complete rock glacier inventories are rare, as most studies focus on individual landforms (e.g. Kääb *et al.*, 1998; Konrad *et al.*, 1999; Scapozza *et al.*, 2014; Monnier and Kinnard, 2017). Using InSAR, Liu *et al.* (2013) survey 59 active rock glaciers in the Californian Sierra Nevada and find average surface velocities of up to 0.84 m year^{-1} in the northern Tien Shan; Wang *et al.* (2017) report more than 80% of mean surface velocities of 170 rock glaciers to remain below 0.60 m year^{-1}, with highest values reaching 1.14 m year^{-1}. Surveying the surface kinematics of 129 rock glaciers in the Austrian Alps with optical feature tracking, Groh and Blöthe (2019) measure mean velocities between 0.11 and 0.29 m year^{-1}, with maximum average displacement of 1.7 m year^{-1}. In comparison, we find 24 rock glaciers with average annual surface displacement >1 m year^{-1} in the Cordón del Plata range, 51 landforms when including ice-debris complexes, suggesting average rates to be systematically higher than in other regions with significant assemblage of periglacial landforms, also in a global context. Among other influencing factors, such as the vertical extent of
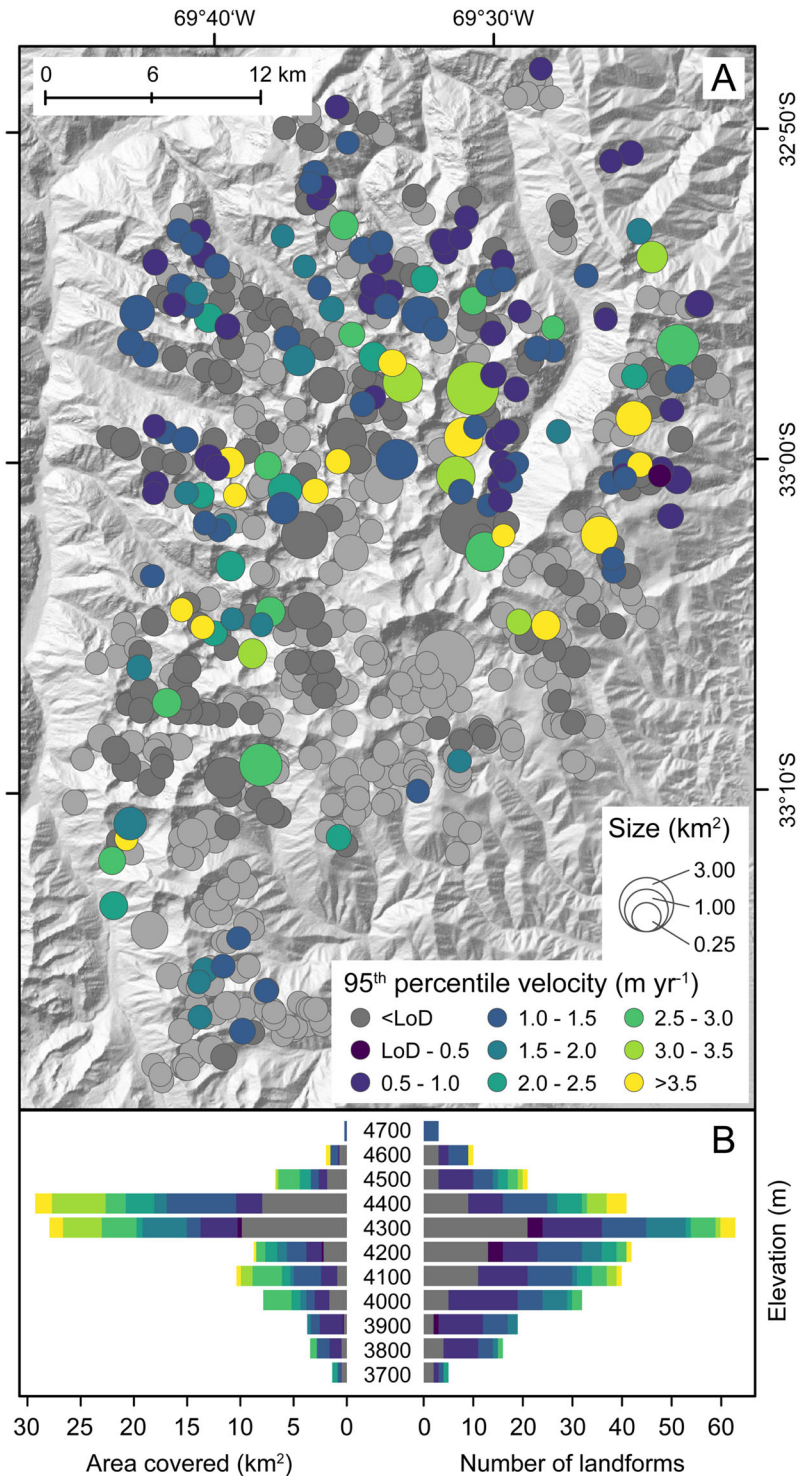
Figure 7. (A) Regional distribution of cryogenic landforms in the Cordón del Plata range successfully tracked from remote sensing imagery ($n = 295$), colour-coded by their 95th percentile surface velocity between 2010 and 2017/18 and scaled to their planimetric area. Light grey colours indicate landforms that were excluded from the analysis, due to unsuccessful feature tracking ($n = 186$). (B) Histograms of area covered (left) and number of landforms (right) colour-coded by their 95th percentile surface velocities for 100 m elevation bins (lower boundary given). Background in (A) from TanDEM-X digital elevation data (© DLR 2017).

the Andean periglacial zone and non-continuous thermal insulation during snow-scarce winters, previous reports of a positive correlation between rock glacier length and flow velocity (Frauenfelder *et al.*, 2003; Janke and Frauenfelder, 2008) might explain systematically higher flow velocities in the Central Andes. Compared to active rock glaciers in the Tyrolean Alps with a mean length and surface area of 451 m and 0.088 km², respectively (Krainer and Ribis, 2012), active rock glaciers in the Cordón del Plata range surpass these dimensions by far, with a mean length of 1102 m and an average area of 0.211

km² (1433 m and 0.419 km², respectively if including ice-debris complexes). This finding is backed by tentative positive correlations between landform size and surface velocity found in this study (Figure 6).

Going beyond average rates for individual landforms by breaking down rock glacier and ice-debris complex polygons into smaller segments along the centreline proves to give valuable insight into the kinematics of periglacial landforms (Figure 4). Segments further allow us to depict the full distribution of velocities perpendicular to the flowline, rather than
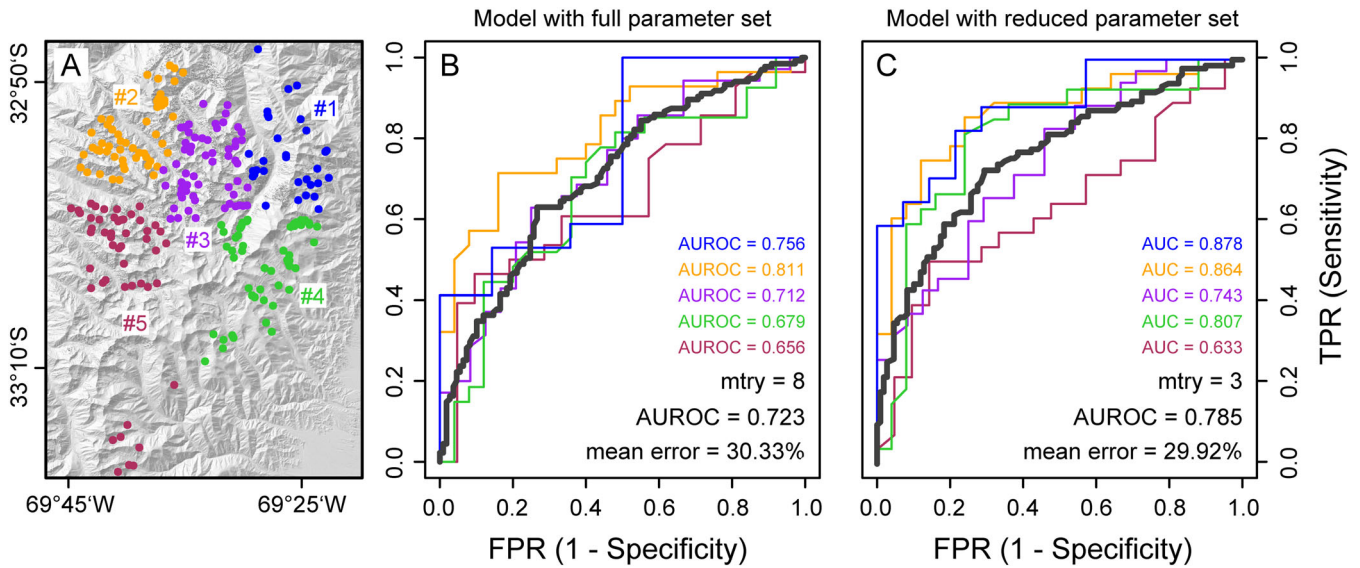
Figure 8. AUROC for landform polygons using spatial cross-validation with five *k*-means clusters of the Cordon del Plata range. (A) Location map of *n* = 244 rock glacier and ice-debris complex polygons, colour-coded by *k*-means spatial clusters: region #1 (blue), region #2 (orange), region #3 (purple), region #4 (green), region #5 (dark red). (B) AUROC for random forest classification using the full parameter set and (C) using the reduced parameter set. Curves in (B) and (C) are colour-coded according to the region left out for spatial cross-validation. Thick grey line gives mean AUROC of 125 model runs; TPR = true positive rate; FPR = false positive rate.

extracting maximum rates along the longitudinal axis (Bodin *et al.*, 2018; Eriksen *et al.*, 2018). Despite the tentative association between surface displacement and local segment slope, we do not find a strong correlation for the entire data set. However, we note here that simple correlations between surface velocities and morphometric variables cannot be expected to reproduce the complex rock glaciers' internal deformation, influenced by material composition, ice temperature and liquid water content (Monnier and Kinnard, 2016; Halla *et al.*, 2020). Nonetheless, the large within-landform heterogeneity of surface deformation, with median rates varying by a factor of three within a few hundred metres (Figure 4), points to the importance of local controls on kinematics and deserves further attention.

With respect to extreme maxima of surface deformation, however, periglacial landforms of the Cordón del Plata range are not exceptional. While our study area hosts several landforms with maximum (95th percentile) displacement surpassing 5 m year^{-1}, maximum velocities reported from other regions are much higher (Delaloye *et al.*, 2010; Eriksen *et al.*, 2018). Yet numerous reports of exceptionally high displacement rates have been reported from out-of-equilibrium rock glaciers that are located close to the lower limit of alpine permafrost where high velocities are often associated with permafrost warming and degradation (Kääb *et al.*, 2007; Bodin *et al.*, 2017; Eriksen *et al.*, 2018; Kellerer-Pirklbauer and Kaufmann, 2018). In contrast, we find the highest displacement rates to cluster in elevations above 4000 m (Figure 7), roughly 300–400 m above the lower limit of permafrost reported for the Cordón del Plata (Barsch and King, 1989; Trombotto *et al.*, 1997; Trombotto and Borzotta, 2009). Yet individual examples of longitudinal profiles indicate elevated rates of movement also close to the terminus of rock glaciers and ice-debris landforms (Figure 4) that might well be associated with warming permafrost temperatures in the region (Trombotto and Borzotta, 2009; Trombotto-Liaudat and Bottegal, 2019).
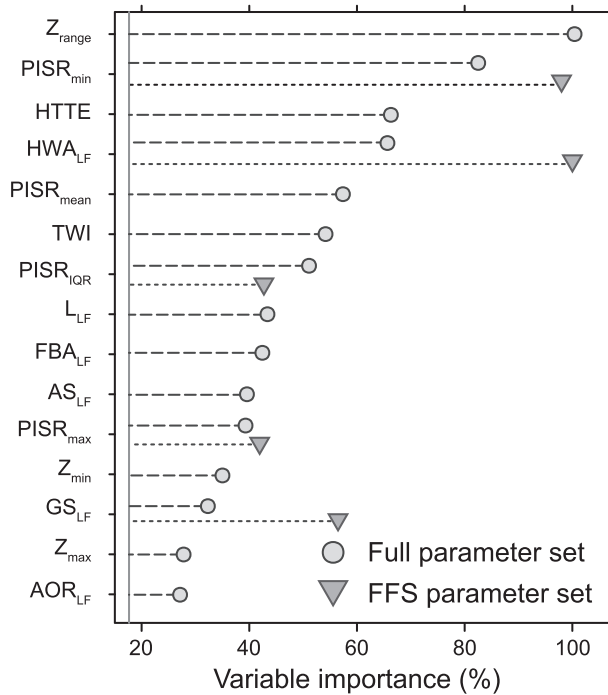

Figure 9. Relative scaled variable importance for random forest classification of landform activity using the full parameter set (points) and a reduced parameter set selected by forward feature selection (triangles). Variable importance given for 15 (of 25) most important parameters for the full parameter set and for 5 (of 8) from the reduced parameter set.

Model performance and controlling factors on different scales

Predicting the state of activity of entire landforms and the segments of rock glaciers and ice-debris complexes using a random forest classification approach with FFS yields moderate to good overall accuracies of 70.08% (mean AUROC = 0.785) and 74.86% (mean AUROC = 0.753), respectively. Though remaining below reported overall accuracies and AUROC values from the Alps that separate active and inactive (Groh and Blöthe, 2019) and intact from relict rock glaciers (Kofler *et al.*, 2020), we point to the fact that our models
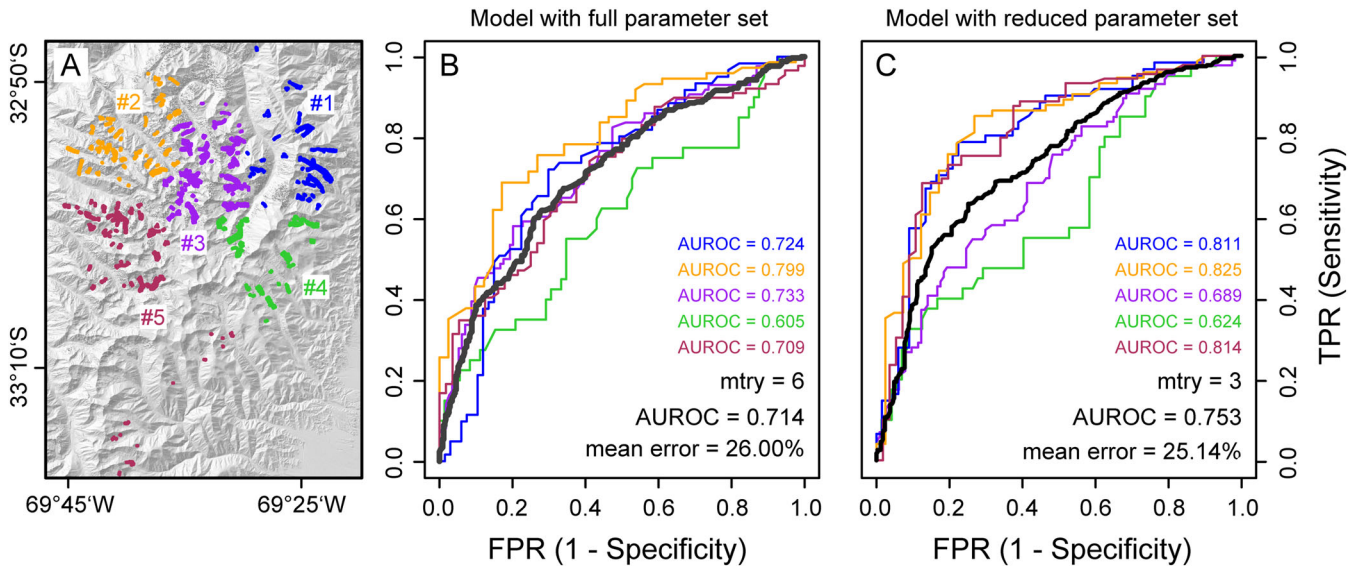
Figure 10. AUROC for landform segments using spatial cross-validation with five *k*-means clusters of the Cordón del Plata range. (A) Location map of *n* = 1020 landform segments, colour-coded by *k*-means spatial clusters: region #1 (blue), region #2 (orange), region #3 (purple), region #4 (green), region #5 (dark red). (B) AUROC for random forest classification using the full parameter set and (C) using the reduced parameter set. Curves in (B) and (C) are colour-coded according to the region left out (LLO-CV) for spatial cross-validation. Thick grey line gives mean AUROC of 125 model runs; TPR = true positive rate; FPR = false positive rate.
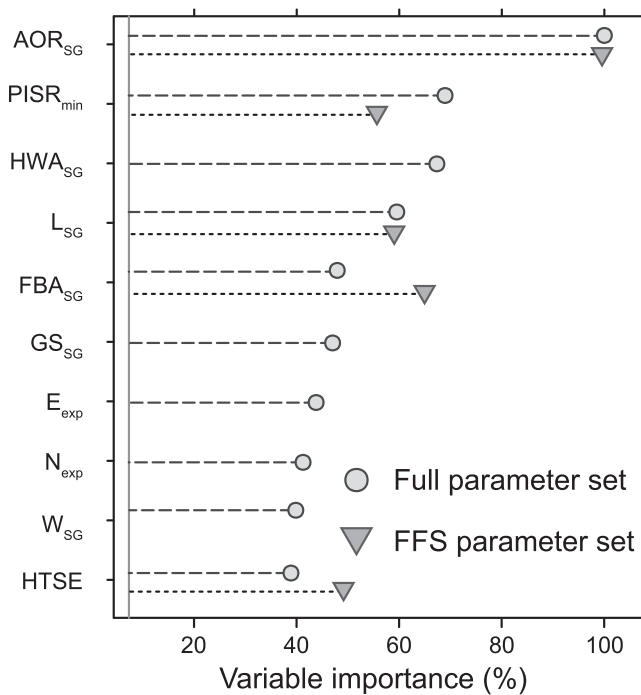

Figure 11. Relative scaled variable importance for random forests classification of landform segment activity using the full parameter set (points) and a reduced parameter set selected by forward feature selection (triangles). Variable importance given for 10 (of 16) most important parameters for the full parameter set and for 5 (of 9) from the reduced parameter set.

perform with satisfying accuracies while encompassing both landform types, rock glaciers and ice-debris complexes. Furthermore, modelling the location of intact rock glaciers in the Central Andes achieved comparable overall accuracies (Brenning and Trombotto, 2006). Spatial cross-validation (i.e. LLO-CV) indicates good transferability between four of five regions for modelling the state of activity of entire landforms; the larger overall LoD (Figure S2), however, might explain the lower performance in region #5.

In line with earlier studies from the Andes (Schrott, 1998; Brenning and Trombotto, 2006) and the European Alps (Groh

and Blöthe, 2019) that stress the significance of solar radiation for permafrost distribution, PISR ranks amongst the highest variable importance values for the distinction between active and inactive landforms in the Cordón del Plata (i.e. exceeding or remaining below the LoD, respectively). Using a similar study design, Groh and Blöthe (2019) find the elevation range and PISR of the landform to have the highest variable importance for the state of activity of rock glaciers in the Kaunertal, Austria. Both variables rank highest for the full parameter set of our study (Figure 9), suggesting that these parameters are very promising predictors for telling

apart active and inactive landforms, independent of the climatic setting.

A comparison between modelling the state of activity of entire landforms and individual landform segments reveals striking differences in the importance of predictor variables on different scales. With the angle of reach and the length position along the flowline amongst the most important variables, geometric parameters seem to dominate the classification on the segment scale (Figure 11) that are, however, less important in the context of classifying the entire landforms. Here, the elevation range and different measures of PISR have higher variable importance (Figure 9). The size of the headwall (i.e. steeply inclined regions of the feeder basin area sourcing debris – HWA_{LF} and HWA_{SG}) and minimum PISR rank among the five most important variables for both entire landforms and the segments. This finding underlines the relevance of material inputs (debris, snow, ice, water) for the activity and spatial distribution of rock glaciers (Janke and Frauenfelder, 2008). Notably, permuting average segment slope and slope statistics for the entire landforms does not reduce the classification accuracy significantly (i.e. has low importance regardless of the tentative qualitative association found between slope and displacement velocity; Figure 7). Despite reports of statistically significant spatial correlations between surface slope and surface velocity (Monnier and Kinnard, 2016; Bodin *et al.*, 2018; Groh and Blöthe, 2019), our findings support the notion that the local stress field might not be the only factor in controlling surface movement at a given location (Frauenfelder *et al.*, 2003). Our results rather point to variables integrating slope and distance to the source (i.e. length position, angle of reach and geometric slope of the landform's segments) to be more powerful predictors on the local scale (Frauenfelder *et al.*, 2003; Janke and Frauenfelder, 2008). In summary, predicting the state of activity for entire landforms and landform segments of rock glaciers and ice-debris complexes points to a scale dependency of controlling variables that calls for further scientific inquiry.

In the light of global warming, rock glaciers became the focus of attention in arid mountain regions, where periglacial landforms proliferate and occupy larger fractions of the landscape than glaciers (IANIGLA, 2018a,b,c). Directly coupled to atmospheric processes, glaciers in the Central Andes of Argentina and Chile showed positive mass balances at the beginning of the 21st century, but shifted to strong negative mass balances after 2010 (Braun *et al.*, 2019; Dussaillant *et al.*, 2019). Projections of warming temperatures will likely shift the 0 °C isotherm upwards by at least 500 m until 2070, leaving more than 50% of rock glaciers contained in the ING for the Central Andes stranded below the future 0 °C isotherm (Drewes *et al.*, 2018). Elevated surface displacements close to the terminus of selected rock glaciers and ice-debris complexes may be induced by warming ice and an increased availability of liquid water that is associated with beginning permafrost degradation reported from this region (Trombotto and Borzotta, 2009; Trombotto-Liaudat and Bottegal, 2019). Future monitoring of surface displacement of a large sample of landforms, as applied in this study, offers a time- and cost-efficient possibility to assess the impact of rising temperatures on the Andean periglacial environment.

Conclusions

Here we present the first study to rigorously quantify and analyse rock glacier and ice-debris complex kinematics of a regional landform inventory in the Central Andes of Argentina. Using a feature-tracking approach in repeated RapidEye satellite imagery, we derive high-resolution 2D velocity fields for 295 landforms in the Cordón del Plata range. Our data show significant surface displacement for 149 of these rock glaciers and ice-debris complexes, with mean velocities between 0.37 and 2.61 m year^{-1}, ranging significantly higher than average speeds of rock glaciers found for inventories in the European Alps, the Tien Shan and the Sierra Nevada. Constructing segments along the centreline of rock glaciers and ice-debris complexes, we shed light on the intra-landform variability of surface movement and observe a tentative association of local slope and velocity. Using a random forest classification approach with FFS, we can predict the state of activity of entire landforms and landform segments with overall accuracies of 70.08% (mean AUROC = 0.785) and 74.86% (mean AUROC = 0.753), respectively. Though the performance of both random forest models is only moderate to good, their variable importance suggests different parameters to control the landforms' state of activity on different spatial scales. On the landform scale, minimum PISR and the elevation range are dominant factors in separating actively moving from inactive landforms, while on the local segment scale, geometric properties like the angle of reach and the length along the flowline come into play. We conclude that feature tracking in optical satellite imagery offers a feasible approach to quantify the kinematics of rock glaciers and ice-debris complexes on a regional basis. Our data contribute to the assessment of the current state of periglacial landforms in the Central Andes and call for further inquiry into the variability of surface deformation on different spatial scales.

Conflict of Interest

The authors declare no competing interests.

Data Availability Statement

The national glacier inventory data of Argentina can be downloaded from http://www.glaciaresargentinos.gob.ar. In the online Supporting Information, we provide a table with all statistics calculated for rock glacier and ice-debris complex polygons and segments that can be linked to the inventory data. Tracked surface velocity rasters will be provided by the corresponding author upon request. The TanDEM-X and RapidEye data were made available to the authors via research proposals that do not allow data sharing.

References

Arenson L, Hoelzle M, Springman S. 2002. Borehole deformation measurements and internal structure of some rock glaciers in Switzerland. *Permafrost and Periglacial Processes* **13**: 117–135. https://doi.org/10.1002/ppp.414

Arenson LU, Jakob M. 2010. The significance of rock glaciers in the dry Andes – a discussion of Azócar and Brenning (2010) and Brenning and Azócar (2010). *Permafrost and Periglacial Processes* **21**: 282–285. https://doi.org/10.1002/ppp.693

Azócar GF, Brenning A. 2010. Hydrological and geomorphological significance of rock glaciers in the dry Andes, Chile (27°–33°S). *Permafrost and Periglacial Processes* 21: 42–53. https://doi.org/10.1002/ppp.669

Barcaza G, Nussbaumer SU, Tapia G, Valdés J, García JL, Videla Y, Albornoz A, Arias V. 2017. Glacier inventory and recent glacier variations in the Andes of Chile, South America. *Annals of Glaciology* 58(75pt2): 166–180.

Barsch D. 1996. *Rockglaciers: Indicators for the Present and Former Geoecology in High Mountain Environments*. Springer: Berlin [online]. Available at: https://doi.org/10.1007/978-3-642-80093-1

Barsch D, King L. 1989. Origin and geoelectrical resistivity of rockglaciers in semi-arid subtropical mountains (Andes of Mendoza, Argentina). *Zeitschrift für Geomorphologie* 33: 151–163.

Berthling I. 2011. Beyond confusion: rock glaciers as cryo-conditioned landforms. *Geomorphology* 131: 98–106. https://doi.org/10.1016/j.geomorph.2011.05.002

Blöthe JH, Rosenwinkel S, Höser T, Korup O. 2019. Rock-glacier dams in High Asia. *Earth Surface Processes and Landforms* 44: 808–824. https://doi.org/10.1002/esp.4532

Bodin X, Krysiecki JM, Schoeneich P, Le Roux O, Lorier L, Echelard T, Peyron M, Walpersdorf A. 2017. The 2006 collapse of the Bérard rock glacier (Southern French Alps). *Permafrost and Periglacial Processes* 28: 209–223. https://doi.org/10.1002/ppp.1887

Bodin X, Rojas F, Brenning A. 2010. Status and evolution of the cryosphere in the Andes of Santiago (Chile, 33.5°S.). *Geomorphology* 118: 453–464. https://doi.org/10.1016/j.geomorph.2010.02.016

Bodin X, Thibert E, Sanchez O, Rabatel A, Jaillet S. 2018. Multi-Annual Kinematics of an Active Rock Glacier Quantified from Very High-Resolution DEMs: An Application-Case in the French Alps. *Remote Sensing* 10(4): 547. https://doi.org/10.3390/rs10040547

Boeckli L, Brenning A, Gruber S, Noetzli J. 2012. A statistical approach to modelling permafrost distribution in the European Alps or similar mountain ranges. *The Cryosphere* 6: 125–140. https://doi.org/10.5194/tc-6-125-2012

Bolch T, Rohrbach N, Kutuzov S, Robson BA, Osmonov A. 2019. Occurrence, evolution and ice content of ice-debris complexes in the Ak-Shiirak, Central Tien Shan revealed by geophysical and remotely-sensed investigations: ice-debris complexes in Ak-Shiirak. *Earth Surface Processes and Landforms* 44: 129–143. https://doi.org/10.1002/esp.4487

Braun MH, Malz P, Sommer C, Farías-Barahona D, Sauter T, Casassa G, Soruco A, Skvarca P, Seehaus TC. 2019. Constraining glacier elevation and mass changes in South America. Nature Climate Change [online]. Available at: http://www.nature.com/articles/s41558-018-0375-7 (accessed 15 January 2019).

Breiman L. 2001. Random forests. *Machine Learning* 45: 5–32. https://doi.org/10.1023/A:1010933404324

Brenning A. 2005. Climatic and geomorphological controls of rock glaciers in the Andes of Central Chile: combining statistical modelling and field mapping, PhD thesis, Humboldt Universität zu Berlin.

Brenning A, Azócar GF. 2010. Statistical analysis of topographic and climatic controls and multispectral signatures of rock glaciers in the dry Andes, Chile (27°-33°S). *Permafrost and Periglacial Processes* 21: 54–66. https://doi.org/10.1002/ppp.670

Brenning A, Long S, Fieguth P. 2012. Detecting rock glacier flow structures using Gabor filters and IKONOS imagery. *Remote Sensing of Environment* 125: 227–237. https://doi.org/10.1016/j.rse.2012.07.005

Brenning A, Trombotto D. 2006. Logistic regression modeling of rock glacier and glacier distribution: topographic and climatic controls in the semi-arid Andes. *Geomorphology* 81: 141–154. https://doi.org/10.1016/j.geomorph.2006.04.003

Castro M, Delgado S, Ferri Hidalgo L, Zalazar L, Falaschi D, Masiokas M, Pecker I, Pitte P, Ruiz L. 2014. *Manual para la realización del Inventario Nacional de Glaciares*. IANIGLA: Mendoza.

Corte A. 1976. The hydrological significance of rock glaciers. *Journal of Glaciology* 17: 157–158. https://doi.org/10.3189/S0022143000030859

Corte A, Espizua LE. 1981. *Inventario de glaciares de la Cuenca del Rio Mendoza*. IANIGLA: Mendoza.

Dall'Asta E, Forlani G, Roncella R, Santise M, Diotri F, Morra di Cella U. 2017. Unmanned aerial systems and DSM matching for rock glacier monitoring. *ISPRS Journal of Photogrammetry and Remote Sensing* 127: 102–114. https://doi.org/10.1016/j.isprsjprs.2016.10.003

Delaloye R, Lambiel C, Gärtner-Roer I. 2010. Overview of rock glacier kinematics research in the Swiss Alps: seasonal rhythm, interannual variations and trends over several decades. *Geographica Helvetica* 65: 135–145.

Drewes J, Moreiras S, Korup O. 2018. Permafrost activity and atmospheric warming in the Argentinian Andes. *Geomorphology* 323: 13–24. https://doi.org/10.1016/j.geomorph.2018.09.005

Dussaillant I, Berthier E, Brun F, Masiokas M, Hugonnet R, Favier V, Rabatel A, Pitte P, Ruiz L. 2019. Two decades of glacier mass loss along the Andes. *Nature Geoscience* 12: 802–808. https://doi.org/10.1038/s41561-019-0432-5

Eriksen HØ, Rouyet L, Lauknes TR, Berthling I, Isaksen K, Hindberg H, Larsen Y, Corner GD. 2018. Recent acceleration of a rock glacier complex, Ádjet, Norway, documented by 62 years of remote sensing observations. *Geophysical Research Letters* [online]. Available at: http://doi.wiley.com/10.1029/2018GL077605 ().

Falaschi D, Castro M, Masiokas M, Tadono T, Ahumada AL. 2014. Rock glacier inventory of the Valles Calchaquíes region (~25°S), Salta, Argentina, derived from ALOS data. *Permafrost and Periglacial Processes* 25: 69–75. https://doi.org/10.1002/ppp.1801

Förstner W. 1986. A feature based correspondence algorithm for image matching. *International Archives of Photogrammetry and Remote Sensing* 26: 150–166.

Frauenfelder R, Haeberli W, Hölzle M. 2003. Rockglacier occurrence and related terrain parameters in a study area of the Eastern Swiss Alps. In *Proceedings of 8th International Conference on Permafrost*, Zurich; 253–258.

Groh T, Blöthe JH. 2019. Rock glacier kinematics in the Kaunertal, Ötztal Alps, Austria. *Geosciences* 9: 373. https://doi.org/10.3390/geosciences9090373

Gruber S. 2012. Derivation and analysis of a high-resolution estimate of global permafrost zonation. *The Cryosphere* 6: 221–233. https://doi.org/10.5194/tc-6-221-2012

Haeberli W. 1985. *Creep of Mountain Permafrost: Internal Structure and Flow of Alpine Rock Glaciers*. ETH Zürich: Zürich.

Haeberli W, Schaub Y, Huggel C. 2017. Increasing risks related to landslides from degrading permafrost into new lakes in de-glaciating mountain ranges. *Geomorphology* 293: 405–417. https://doi.org/10.1016/j.geomorph.2016.02.009

Haeberli W, Hallet B, Arenson L, Elconin R, Humlum O, Kääb A, Kaufmann V, Ladanyi B, Matsuoka N, Springman S, Vonder Mühll D. 2006. Permafrost creep and rock glacier dynamics. *Permafrost and Periglacial Processes* 17: 189–214. https://doi.org/10.1002/ppp.561

Halla C, Blöthe JH, Tapia Baldis C, Trombotto D, Hilbich C, Hauck C, Schrott L. 2020. Ice content and interannual water storage changes of an active rockglacier in the dry Andes of Argentina. *The Cryosphere Discussion* [online]. Available at: https://www.the-cryosphere-discuss.net/tc-2020-29/ ().

Heredia N, Farias P, García-Sansegundo J, Giambiagi L. 2012. The basement of the Andean Frontal Cordillera in the Cordón del Plata (Mendoza, Argentina): geodynamic evolution. *Andean Geology* 39: 242–257.

Humlum O. 2000. The geomorphic significance of rock glaciers: estimates of rock glacier debris volumes and headwall recession rates in West Greenland. *Geomorphology* 35: 41–67. https://doi.org/10.1016/S0169-555X(00)00022-2

IANIGLA. 2018a. Inventario Nacional de Glaciares: Informe de la subcuenca del río Las Tunas y arroyos Anchayuyo, Grande y Manzano (Tunuyán norte). In *Cuenca del río Tunuyán*. Ministerio de Ambiente y Desarrollo Sustentable de la Nación: IANIGLA-CONICET.

IANIGLA. 2018b. Inventario Nacional de Glaciares: Informe de la subcuenca del río Tupungato. Cuenca del río Mendoza. In *Cuenca del río Mendoza*. Ministerio de Ambiente y Desarrollo Sustentable de la Nación: IANIGLA-CONICET.

IANIGLA. 2018c. Inventario Nacional de Glaciares: Informe de las subcuencas de los ríos Blancos y Sector del Cordón del Plata. In *Cuenca del río Mendoza*. Ministerio de Ambiente y Desarrollo Sustentable de la Nación: IANIGLA-CONICET.

IANIGLA. 2018d. *Inventario Nacional de Glaciares*. IANIGLA: Mendoza.

James G, Witten D, Hastie T, Tibshirani R (eds). 2013. *An Introduction to Statistical Learning: With Applications in R*. Springer: New York.

Janke J, Frauenfelder R. 2008. The relationship between rock glacier and contributing area parameters in the Front Range of Colorado. *Journal of Quaternary Science* **23**: 153–163. https://doi.org/10.1002/jqs.1133

Janke JR, Bellisario AC, Ferrando FA. 2015. Classification of debris-covered glaciers and rock glaciers in the Andes of Central Chile. *Geomorphology* **241**: 98–121. https://doi.org/10.1016/j.geomorph.2015.03.034

Jones DB, Harrison S, Anderson K, Betts RA. 2018. Mountain rock glaciers contain globally significant water stores. *Scientific Reports* **8**: 1–10. https://doi.org/10.1038/s41598-018-21244-w

Kääb A, Frauenfelder R, Roer I. 2007. On the response of rockglacier creep to surface temperature increase. *Global and Planetary Change* **56**: 172–187. https://doi.org/10.1016/j.gloplacha.2006.07.005

Kääb A, Gudmundsson G, Hölzle M. 1998. Surface deformation of creeping mountain permafrost: photogrammetric investigations on rock glacier Murtèl, Swiss Alps, paper presented at the *7th International Permafrost Conference*.

Kääb A, Kaufmann V, Ladstädter R, Eiken T. 2003. Rock glacier dynamics: implications from high-resolution measurements of surface velocity fields, paper presented at the *8th International Permafrost Conference*.

Kääb A, Vollmer M. 2000. Surface geometry, thickness changes and flow fields on creeping mountain permafrost: automatic extraction by digital image analysis. *Permafrost and Periglacial Processes* **11**: 315–326. https://doi.org/10.1002/1099-1530(200012)11:4<315::AID-PPP365>3.0.CO;2-J.

Kaser G, Grosshauser M, Marzeion B. 2010. Contribution potential of glaciers to water availability in different climate regimes. *Proceedings of the National Academy of Sciences* **107**: 20 223–20 227. https://doi.org/10.1073/pnas.1008162107

Kellerer-Pirklbauer A, Kaufmann V. 2018. Deglaciation and its impact on permafrost and rock glacier evolution: new insight from two adjacent cirques in Austria. *Science of The Total Environment* **621**: 1397–1414. https://doi.org/10.1016/j.scitotenv.2017.10.087

Kenner R, Phillips M, Beutel J, Hiller M, Limpach P, Pointner E, Volken M. 2017. Factors controlling velocity variations at short-term, seasonal and multiyear time scales, Ritigraben rock glacier, Western Swiss Alps: factors driving rock glacier velocity at three time scales. *Permafrost and Periglacial Processes* **28**: 675–684. https://doi.org/10.1002/ppp.1953

Kienholz C, Rich JL, Arendt AA, Hock R. 2014. A new method for deriving glacier centerlines applied to glaciers in Alaska and northwest Canada. *The Cryosphere* **8**: 503–519. https://doi.org/10.5194/tc-8-503-2014

Kofler C, Steger S, Mair V, Zebisch M, Comiti F, Schneiderbauer S. 2020. An inventory-driven rock glacier status model (intact vs. relict) for South Tyrol, Eastern Italian Alps. *Geomorphology* **350**: 106887. https://doi.org/10.1016/j.geomorph.2019.106887

Konrad SK, Humphrey NF, Steig EJ, Clark DH, Potter N, Pfeffer WT. 1999. Rock glacier dynamics and paleoclimatic implications. *Geology* **27**: 1131–1134. https://doi.org/10.1130/0091-7613(1999)027<1131:RGDAPI>2.3.CO;2

Krainer K, Mostler W. 2006. Flow velocities of active rock glaciers in the Austrian Alps. *Geografiska Annaler, Series A, Physical Geography* **88**(4): 267–280.

Krainer K, Ribis M. 2012. A rock glacier inventory of the Tyrolean Alps (Austria). *Austrian Journal of Earth Sciences* **105**: 32–47.

Kuhn M. 2008. Building Predictive Models inRUsing thecaretPackage. *Journal of Statistical Software*, **28**(5). https://doi.org/10.18637/jss.v028.i05

Kummert M, Delaloye R. 2018. Mapping and quantifying sediment transfer between the front of rapidly moving rock glaciers and torrential gullies. *Geomorphology* **309**: 60–76. https://doi.org/10.1016/j.geomorph.2018.02.021

Liaw A, Wiener M. 2002. Classification and regression by randomForest. *R News* **2**: 18–22.

Liu L, Millar CI, Westfall RD, Zebker HA. 2013. Surface motion of active rock glaciers in the Sierra Nevada, California, USA: inventory and a case study using InSAR. *The Cryosphere* **7**: 1109–1119. https://doi.org/10.5194/tc-7-1109-2013

Liu Q, Mayer C, Wang X, Nie Y, Wu K, Wei J, Liu S. 2020. Interannual flow dynamics driven by frontal retreat of a lake-terminating glacier in the Chinese Central Himalaya. *Earth and Planetary Science Letters* **546**: 116450. https://doi.org/10.1016/j.epsl.2020.116450

Luckman A, Quincey D, Bevan S. 2007. The potential of satellite radar interferometry and feature tracking for monitoring flow rates of Himalayan glaciers. *Remote Sensing of Environment* **111**: 172–181. https://doi.org/10.1016/j.rse.2007.05.019

Meyer H, Reudenbach C, Hengl T, Katurji M, Nauss T. 2018. Improving performance of spatio-temporal machine learning models using forward feature selection and target-oriented validation. *Environmental Modelling & Software* **101**: 1–9. https://doi.org/10.1016/j.envsoft.2017.12.001

Monnier S, Kinnard C. 2015. Reconsidering the glacier to rock glacier transformation problem: new insights from the Central Andes of Chile. *Geomorphology* **238**: 47–55.

Monnier S, Kinnard C. 2016. Interrogating the time and processes of development of the Las Liebres rock glacier, Central Chilean Andes, using a numerical flow model. *Earth Surface Processes and Landforms* **41**: 1884–1893. https://doi.org/10.1002/esp.3956

Monnier S, Kinnard C. 2017. Pluri-decadal (1955–2014) evolution of glacier–rock glacier transitional landforms in the Central Andes of Chile (30–33°S). *Earth Surface Dynamics* **5**: 493–509. https://doi.org/10.5194/esurf-5-493-2017

Montgomery DR, Balco G, Willett SD. 2001. Climate, tectonics, and the morphology of the Andes. *Geology* **29**: 579–582. https://doi.org/10.1130/0091-7613(2001)029<0579.

Paskoff R. 1970. *Recherche morphologiques dans le Chili semi-aride*. Bordeaux: Biscaye Frères.

Potter N. 1972. Ice-cored rock glacier, Galena Creek, Northern Absaroka Mountains, Wyoming. *Geological Society of America Bulletin* **83**(10): 3025–3058. https://doi.org/10.1130/0016-7606(1972)83[3025:IRGGCN]2.0.CO;2

Pourrier J, Jourde H, Kinnard C, Gascoin S, Monnier S. 2014. Glacier meltwater flow paths and storage in a geomorphologically complex glacial foreland: the case of the Tapado glacier, dry Andes of Chile (30°S). *Journal of Hydrology* **519**: 1068–1083.

Rangecroft S, Harrison S, Anderson K, Magrath J, Castel AP, Pacheco P. 2013. Climate change and water resources in arid mountains: an example from the Bolivian Andes. *AMBIO* **42**: 852–863. https://doi.org/10.1007/s13280-013-0430-6

Rau F, Mauz F, Vogt S, Khalsa SJ, Raup B. 2005. Illustrated GLIMS Glacier Classification Manual – Glacier Classification Guidance for the GLIMS Glacier Inventory. IPG: Freiburg.

Saito K, Trombotto Liaudat D, Yoshikawa K, Mori J, Sone T, Marchenko S, Romanovsky V, Walsh J, Hendricks A, Bottegal E. 2016. Late Quaternary permafrost distributions downscaled for South America: examinations of GCM-based maps with observations: South American permafrost distribution in the Late Quaternary. *Permafrost and Periglacial Processes* **27**: 43–55. https://doi.org/10.1002/ppp.1863

Scapozza C, Lambiel C, Bozzini C, Mari S, Conedera M. 2014. Assessing the rock glacier kinematics on three different timescales: a case study from the southern Swiss Alps. *Earth Surface Processes and Landforms* **39**: 2056–2069. https://doi.org/10.1002/esp.3599

Schaffer N, MacDonell S, Réveillet M, Yáñes E, Valois R. 2019. Rock glaciers as a water resource in a changing climate in the semiarid Chilean Andes. *Regional Environmental Change* **19**: 1263–1279. https://doi.org/10.1007/s10113-018-01459-3

Schrott L. 1998. The hydrological significance of high mountain permafrost and its relation to solar radiation, a case study in the high Andes of San Juan, Argentina. *Bamberger Geographische Schriften* **15**: 71–84.

Schrott L, Otto JC, Keller F. 2012. Modelling alpine permafrost distribution in the Hohe Tauern region, Austria. *Austrian Journal of Earth Sciences* **105**: 169–183.

Schwalbe E, Maas H-G. 2017. Determination of high resolution spatio-temporal glacier motion fields from time-lapse sequences. *Earth Surface Dynamics Discussions*: 1–30. https://doi.org/10.5194/esurf-2017-33

Scotti R, Brardinoni F, Alberti S, Frattini P, Crosta GB. 2013. A regional inventory of rock glaciers and protalus ramparts in the central Italian

Alps. *Geomorphology* **186**: 136–149. https://doi.org/10.1016/j.geomorph.2012.12.028

Strozzi T, Caduff R, Jones N, Barboux C, Delaloye R, Bodin X, Kääb A, Mätzler E, Schrott L. 2020. Monitoring rock glacier kinematics with satellite synthetic aperture radar. *Remote Sensing* **12**: 559. https://doi.org/10.3390/rs12030559

Planet Team. 2018. Planet Application Program Interface: In Space for Life on Earth. San Francisco [online] Available from: https://api.planet.com

Trombotto D, Borzotta E. 2009. Indicators of present global warming through changes in active layer-thickness, estimation of thermal diffusivity and geomorphological observations in the Morenas Coloradas rockglacier, Central Andes of Mendoza, Argentina. *Cold Regions Science and Technology* **55**: 321–330. https://doi.org/10.1016/j.coldregions.2008.08.009

Trombotto D, Buk E, Hernández J. 1997. Monitoring of mountain permafrost in the Central Andes, Cordon del Plata, Mendoza, Argentina. *Permafrost and Periglacial Processes* **8**: 123–129.

Trombotto Liaudat D, Sileo N, Dapeña C. 2020. Periglacial water paths within a rock glacier-dominated catchment in the Stepanek area, Central Andes, Mendoza, Argentina. *Permafrost and Periglacial Processes* **31**: 311–323. https://doi.org/10.1002/ppp.2044

Trombotto-Liaudat D, Bottegal E. 2019. Recent evolution of the active layer in the Morenas Coloradas rock glacier, Central Andes, Mendoza, Argentina and its relation with kinematics. *Cuadernos de Investigación Geográfica* [online]. Available at: https://publicaciones.unirioja.es/ojs/index.php/cig/article/view/3946 ().

Villarroel C, Tamburini Beliveau G, Forte A, Monserrat O, Morvillo M. 2018. DInSAR for a regional inventory of active rock glaciers in the dry Andes mountains of Argentina and Chile with Sentinel-1 data. *Remote Sensing* **10**: 1588. https://doi.org/10.3390/rs10101588

Vivero S, Lambiel C. 2019. Monitoring the crisis of a rock glacier with repeated UAV surveys. *Geographica Helvetica* **74**: 59–69. https://doi.org/10.5194/gh-74-59-2019

Viviroli D, Weingartner R. 2004. The hydrological significance of mountains: from regional to global scale. *Hydrology and Earth System Sciences* **8**: 1017–1030. https://doi.org/10.5194/hess-8-1017-2004

Viviroli D, Archer DR, Buytaert W, Fowler HJ, Greenwood GB, Hamlet AF, Huang Y, Koboltschig G, Litaor MI, Lopez-Moreno JI, Lorentz S, Schadler B, Schreier H, Schwaiger K, Vuille M, Woods R. 2011. Climate change and mountain water resources: overview and recommendations for research, management and policy. *Hydrology and Earth System Sciences* **15**: 471–504. https://doi.org/10.5194/hess-15-471-2011

Wang X, Liu L, Zhao L, Wu T, Li Z, Liu G. 2017. Mapping and inventorying active rock glaciers in the northern Tien Shan of China using satellite SAR interferometry. *The Cryosphere* **11**: 997–1014. https://doi.org/10.5194/tc-11-997-2017

Wirz V, Gruber S, Purves RS, Beutel J, Gärtner-Roer I, Gubler S, Vieli A. 2016. Short-term velocity variations at three rock glaciers and their relationship with meteorological conditions. *Earth Surface Dynamics* **4**: 103–123. https://doi.org/10.5194/esurf-4-103-2016

Supporting Information

Additional supporting information may be found online in the Supporting Information section at the end of the article.

Figure S1. Comparison between TanDEM-X digital elevation model (top) and SRTM digital elevation model (bottom). All panels show the same subset of the Cordón del Plata study region with superimposed rock glacier inventory outlines (black). Left column shows hillshade view, while right column depicts terrain roughness calculated as the standard deviation of values within a circular window with 100 m diameter of a 3 × 3 pixel slope raster.

Figure S2. Study area with 28 grid subsets used for feature tracking in RapidEye satellite imagery colour-coded by respective level of detection (LoD) for each rectangle (Table S1). Superimposed are rock glacier polygons from the national inventory in grey and rounded LoD values in black/white.

Figure S3. Horizontal surface movement of the Stepanek ice-debris complex, as determined by (a) repeated dGNSS surveys of 23 ground control points in 2018 and 2019, (b) feature tracking of repeated unmanned aerial vehicle (UAV)-derived digital elevation models in 2018 and 2019, and (c) feature tracking in RapidEye satellite imagery from 2010 and 2018. (d) Comparison between dGNSS-measured velocities for 2018–2019 and the velocities estimated by feature tracking in UAV-derived elevation data for 2018–2019 (red) and RapidEye imagery for 2010–2018 (blue), respectively. For both, residual standard error (RSE) and mean absolute error (MAE) are given to quantify deviation from the 1:1 line.

Table S1. Acquisition date and rounded errors for the 28 grid subsets used for feature tracking in RapidEye satellite imagery and UAV imagery. Where grid subsets were covered by both sets of repeated imagery, those results with larger LoD have been rejected (in grey italics below).

Table S2. Velocity distributions for 149 polygons with displacement larger than LoD.